

1 Development of global temperature and pH calibrations based 2 on bacterial 3-hydroxy fatty acids in soils

3
4 Pierre Véquaud¹, Sylvie Derenne¹, Alexandre Thibault², Christelle Anquetil¹, Giuliano
5 Bonanomi³, Sylvie Collin¹, Sergio Contreras⁴, Andrew T. Nottingham^{5,6}, Pierre Sabatier⁷,
6 Norma Salinas⁸, Wesley Phillip Scott⁹, Josef P. Werne⁹, Arnaud Huguet¹

7
8 ¹Sorbonne Université, CNRS, EPHE, PSL, UMR METIS, Paris, 75005, France

9 ²Antea Group, Innovation Hub, 803 boulevard Duhamel du Monceau, Olivet, 45160, France

10 ³Dipartimento di Agraria, Università di Napoli Federico II, via Università 100, Portici, NA, 80055, Italy

11 ⁴Laboratorio de Ciencias Ambientales (LACA), Departamento de Química Ambiental, Facultad de Ciencias &
12 Centro de Investigación en Biodiversidad y Ambientes Sustentables (CIBAS), Universidad Católica de la
13 Santísima Concepción, Casilla 297, Concepción, Chile

14 ⁵School of Geosciences, University of Edinburgh, Crew Building, Kings Buildings, Edinburgh EH9 3FF United
15 Kingdom

16 ⁶School of Geography, University of Leeds, Leeds, United Kingdom

17 ⁷Univ. Savoie Mont Blanc, CNRS, EDYTEM, Le Bourget du Lac, 73776, France

26 ⁸Instituto de Ciencias de la Naturaleza, Territorio y Energías Renovables, Pontificia Universidad Católica del Perú,
27 Av. Universitaria 1801, San Miguel, Lima 32, Peru

28 ⁹Department of Geology and Environmental Science, University of Pittsburgh, Pittsburgh, PA 15260, USA

29

30 *Correspondence to:* Arnaud Huguet (arnaud.huguet@sorbonne-universite.fr)

31 **Abstract.** 3-hydroxy fatty acids (3-OH FAs) with 10 to 18 C atoms are membrane lipids mainly
32 produced by Gram-negative bacteria. They have been recently proposed as temperature and pH
33 proxies in terrestrial settings. Nevertheless, the existing correlations between pH/temperature
34 and indices derived from 3-OH FA distribution (RIAN, RAN₁₅ and RAN₁₇) are based on a small
35 soil dataset (ca. 70 samples) and only applicable regionally. The aim of this study was to
36 investigate the applicability of 3-OH FAs as mean annual air temperature (MAAT) and pH
37 proxies at the global level. This was achieved using an extended soil dataset of 168 topsoils
38 distributed worldwide, covering a wide range of temperatures (5°C to 30°C) and pH (3 to 8).
39 The response of 3-OH FAs to temperature and pH was compared to that of established branched
40 GDGT-based proxies (MBT'_{5Me}/CBT). Strong linear relationships between 3-OH FA-derived
41 indices (RAN₁₅, RAN₁₇ and RIAN) and MAAT/pH could only be obtained locally, for some of
42 the individual transects. This suggests that these indices cannot be used as paleoproxies at the
43 global scale using simple linear regression models, in contrast with the MBT'_{5Me} and CBT.
44 However, strong global correlations between 3-OH FA relative abundances and MAAT/pH
45 were shown by using other algorithms (multiple linear regression, k-NN and random forest
46 models). The applicability of the three aforementioned models for paleotemperature
47 reconstruction was tested and compared with the MAAT record from a Chinese speleothem.

48 The calibration based on the random forest model appeared to be the most robust. It generally
49 showed similar trends with previously available records and highlighted known climatic events
50 poorly visible when using local 3-OH FA calibrations. Altogether, these results demonstrate
51 the potential of 3-OH FAs as paleoproxies in terrestrial settings.

52

53 **Keywords:** 3-hydroxy fatty acids; branched GDGTs; soils; global calibration; temperature and
54 pH proxy

55

56

1. Introduction

58 Investigating past climate variations is essential to understand and predict future
59 environmental changes, especially in the context of global anthropogenic change. Direct
60 records of environmental parameters are available for the last decades, the so-called
61 "instrumental" period. Beyond this period, proxies can be used to obtain indirect information
62 on environmental parameters. A major challenge is to develop reliable proxies which can be
63 applied to continental environments in addition to marine ones. Indeed, available proxies have
64 been mainly developed and used in marine settings, as the composition and mechanism of
65 formation of marine sedimentary cores is less complex than in continental settings, which are
66 highly heterogeneous. Several environmental proxies based on organic (e.g. the alkenone
67 unsaturation index ($U^{k'37}$; Brassell et al., 1986) and inorganic (Mg/Ca ratio and $^{18}\text{O}/^{16}\text{O}$ ratio of
68 foraminifera; Emiliani, 1955; Erez and Luz, 1983) fossil remains were notably developed for
69 the reconstruction of sea surface temperatures.

70 Some of the existing proxies are based on membrane lipids synthesized by certain
71 microorganisms (Eglinton and Eglinton, 2008; Schouten et al., 2013). These microorganisms
72 are able to adjust the composition of their membrane lipids in response to the prevailing
73 environmental conditions in order to maintain an appropriate fluidity and to ensure the optimal
74 state of the cellular membrane (Singer and Nicolson, 1972; Sinensky, 1974; Hazel and
75 Williams, 1990; Denich et al., 2003). The structure of glycerol dialkyl glycerol tetraethers
76 (GDGTs), which are membrane lipids biosynthesized by archaea and some bacteria, is
77 especially known to be related to environmental conditions. Archaeal GDGTs are constituted
78 of isoprenoid alkyl chains ether-linked to glycerol, whereas bacterial GDGTs are characterized
79 by branched alkyl chains instead of isoprenoid ones. The latter compounds are ubiquitous in
80 terrestrial (Weijers et al., 2007; Peterse et al., 2012; De Jonge et al., 2014; Naafs et al., 2017)
81 and aquatic environments (Peterse et al., 2009; Tierney and Russell, 2009; Sinninghe Damsté
82 et al., 2009; Loomis et al., 2012; Peterse et al., 2015; Weber et al., 2015). These branched
83 GDGTs (brGDGTs) are produced by still unidentified bacteria, although some of them may
84 belong to the phylum *Acidobacteria* (Sinninghe Damsté et al., 2011, 2014, 2018). The analysis
85 of brGDGTs in a large number of soils distributed worldwide showed that the relative
86 distribution of these compounds is mainly related to mean annual air temperature (MAAT) and
87 soil pH (Weijers et al., 2007; Peterse et al., 2012; De Jonge et al., 2014). Even though brGDGT
88 proxies were largely investigated over the last 10 years (De Jonge et al., 2014; Dearing
89 Crampton-Flood et al., 2020) and were applied to various paleorecords (e.g. Coffinet et al.,

90 2018; Wang et al., 2020), new molecular proxies, independent of and complementary to
91 brGDGTs, are needed to improve the reliability of temperature reconstructions in terrestrial
92 settings.

93 Recent studies have unveiled the potential of another family of bacterial lipids – 3-
94 hydroxy fatty acids (3-OH FAs) – for temperature and pH reconstructions in terrestrial (Wang
95 et al., 2016, 2018; Huguet et al., 2019) and marine (Yang et al., 2020) settings. 3-OH FAs with
96 10 to 18 carbon atoms are specifically produced by Gram-negative bacteria and are bound to
97 the lipopolysaccharide (LPS) by ester or amide bonds (Wollenweber et al., 1982; Wollenweber
98 and Rietschel, 1990). Three types of 3-OH FAs can be distinguished, with either *normal* chains
99 or branched chains, *iso* or *anteiso*.

100 The analysis of 3-OH FAs in soils showed that the ratio of C₁₅ or C₁₇ *anteiso* 3-OH
101 FA to *normal* C₁₅ or C₁₇ 3-OH FA (RAN₁₅ and RAN₁₇ indices, respectively) were negatively
102 correlated with MAAT along the three mountains investigated so far: Mts. Shennongjia (China;
103 Wang et al., 2016), Rungwe and Majella (Tanzania and Italy, respectively; Huguet et al., 2019).
104 This suggests that Gram-negative bacteria producing these fatty acids respond to colder
105 temperatures with an increase in *anteiso*-C₁₅/C₁₇ vs. *n*-C₁₅/C₁₇ 3-OH FAs, in order to maintain
106 a proper fluidity and optimal state of the bacterial membrane, the so-called homeoviscous
107 adaptation mechanism (Sinensky, 1974; Hazel and Eugene Williams, 1990). Nevertheless, the
108 relationships between RAN₁₅ and MAAT along the three mountain transects showed the same
109 slopes but different intercepts (Wang et al., 2016; Huguet et al., 2019), suggesting that regional
110 or local RAN₁₅ relations may be more appropriate to apply for temperature reconstructions in
111 terrestrial settings. In contrast, a significant calibration between RAN₁₇ and MAAT could be
112 established using combined data from the three mountain regions (Wang et al., 2016; Huguet
113 et al., 2019).

114 Another index, defined as the cologarithm of the sum of *anteiso* and *iso* 3-OH FAs
115 divided by the sum of *normal* homologues (RIAN index), was shown to be strongly negatively
116 correlated with soil pH along the three aforementioned mountains (Wang et al., 2016; Huguet
117 et al., 2020), reflecting a general relative increase in normal homologues compared to branched
118 (*iso* and *anteiso*) ones with increasing pH. This mechanism was suggested to reduce the
119 permeability and fluidity of the membrane for the cell to cope with lower pH (Russell et al.,
120 1995; Denich et al., 2003; Beales, 2004).

121 3-OH FA indices were recently applied for the first time to the reconstruction of the
122 temperature and hydrological changes over the last 10,000 years in a speleothem from China
123 (Wang et al., 2018), showing the potential of 3-OH FAs as independent tools for environmental

124 reconstruction in terrestrial settings. A very recent study based on marine sediments from the
125 North Pacific Ocean suggested that the distribution of 3-OH FAs could also be used to
126 reconstruct sea surface temperature (Yang et al., 2020).

127 Even though these results are promising, the linear regressions between pH/MAAT and
128 3-OH FA indices in terrestrial environments are still based on a rather small dataset (ca. 70 soil
129 samples; Wang et al., 2016; Huguet et al., 2019). The aim of this study was to investigate the
130 applicability of 3-OH FAs as MAAT and pH proxies at the global level using an extended soil
131 dataset and refined statistical tools. 3-OH FA distribution from 54 soils was determined in four
132 globally distributed altitudinal transects (Tibet, Italy, Peruvian Andes and Chile) and was
133 combined with data previously published by Wang et al. (2016; Mt Shennongjia, China),
134 Huguet et al. (2019; Mt. Rungwe, Tanzania and Mt. Majella, Italy) and Véquaud et al. (2021;
135 Mts. Lautaret-Bauges, France), leading to a total of 168 samples. In addition to linear
136 regressions, non-parametric, machine learning models were used to improve the global
137 relationships between 3-OH FA distribution and MAAT/pH. These models present the
138 advantage of taking into account non-linear environmental influences, in line with the intrinsic
139 complexity of the environmental settings. Finally, these new models were tested and compared
140 by applying them to a speleothem archive (Wang et al., 2018) representing to date the only
141 available MAAT record derived from 3-OH FA proxies in continental setting. As brGDGTs are
142 the only microbial organic proxies which can be used for temperature and pH reconstructions
143 in terrestrial settings so far, they can serve as a reference proxy to understand the temperature
144 and pH dependency of 3-OH FAs analyzed in the same dataset. 3-OH FAs and brGDGTs have
145 thus been concomitantly analyzed to assess their reliability and complementarity as independent
146 temperature and pH proxies.

147

148

149 **2. Material and methods**

150 **2.1. Soil dataset**

151 *2.1.1. Study sites*

152 The dataset of the present study is comprised of the globally distributed surface soils
153 previously analyzed for brGDGTs and 3-OH FAs and collected along 4 altitudinal transects:
154 Mts. Shennongjia (China; Yang et al., 2015; Wang et al., 2016), Rungwe (Tanzania; Coffinet
155 et al., 2017; Huguet et al., 2019), Majella (Italy; Huguet et al., 2019) and Lautaret-Bauges

156 (France; Véquaud et al., 2021). This set was extended with surficial soils (0-10 cm) from 4
157 additional altitudinal transects described below, located in Italy, Tibet, Peru and Chile (Table
158 1).

159 Soil samples were collected from 13 sites along Mount Pollino in the Calabria region
160 (Italy) between 0 and 2,200 m above sea level (a.s.l.) (Table 1). Mt. Pollino is located in the
161 calcareous Apennine range and is 2,248 m a.s.l. It is framed to the northwest by the Sierra de
162 Prete (2,181 m high) and to the south by the Pollino Abyss. The alpine to subalpine area (above
163 2,100 m a.s.l.) is characterized by the presence of Mediterranean grasslands (*Festuca bosniaca*,
164 *Carex kitaibeliana*) and the presence of sinkholes (Todaro et al., 2007; Scalercio et al., 2014).
165 The mountainous vegetation (over 1,200 m a.s.l.) is dominated by *Fagus sylvatica* forests and,
166 at the treeline, by scattered *Pinus leucodermis* (Bonanomi et al., 2020). The soil is poorly
167 developed and dominated by calcareous soils. Between 0 to 1,200 m a.s.l (Scalercio et al., 2014
168 and reference therein), Mt. Pollino is characterized by the presence of *Q. ilex* forests or shrubs.
169 Climate along this mountain is humid Mediterranean, with high summer temperatures and an
170 irregular distribution of rainfall throughout the year with pronounced summer drought (39.5%
171 in winter, 23.7% in spring, 29.2% in autumn, 7.6% in summer; average annual precipitation:
172 1,570 mm; see Todaro et al., 2007). MAAT is comprised between 7 °C (2,200 m a.s.l) and 18
173 °C (0 m a.s.l; Scalercio et al., 2014). MAAT along Mt. Pollino was estimated using a linear
174 regression between two MAAT (16°C at 400 m a.s.l and 10°C at 1,600 m a.s.l.) from the
175 meteorological data (Castrovilliari station) recorded by Scalercio et al. (2014). The pH of the
176 soils analyzed in the present study ranges between 4.5 and 6.8 (Table 1).

177 Soil samples were collected from 17 sites along Mount Shegyla between 3,106 and
178 4,474 m a.s.l. (southeastern Tibet, China), as previously described by Wang et al. (2015).
179 Different climatic zonations are observed along this high-altitude site (2,700 to 4,500 m a.s.l):
180 (i) a mountainous temperate zone between 2,700 and 3,400 m, (ii) a subalpine cold temperate
181 zone between 3,400 and 4,300 m and (iii) a cold alpine zone above 4,300 m. Plant species, such
182 as brown oak (*Q. semecarpifolia*) or common fir (*Abies alba*) are abundant within the
183 mountainous and subalpine levels. In the cold subalpine zone, the Forrest's fir (*Abies georgei*
184 var. *smithii*) is endemic to western China. In the cold alpine zone, coniferous species (*Sabina*
185 *saltuaria*) as well as species typical of mountainous regions such as *Rhododendron* are
186 observed. MAAT was estimated using a linear regression between 7 measured MAAT from the
187 data recorded by Wang et al. (2015). The average MAAT along the transect is 4.6°C, with a
188 minimum of 1.1 °C at ca. 4,500 m a.s.l. and a maximum of 8.9 °C at ca. 3,100 m a.s.l. (Table
189 1). Soil pH ranges between 4.6 and 6.4 (Table 1).

190 Soils were sampled from 14 sites in the Peruvian Andes along the Kosñipata transect,
191 located in south-eastern Peru, in the upper part of the Madre de Dios/Madeira watershed, east
192 of the Andes Cordillera (Nottingham et al., 2015). This transect (190 m to 3,700 m a.s.l) is well-
193 documented and is the object of numerous ecological studies (Malhi et al., 2010; Nottingham
194 et al., 2015). There is a shift in vegetation zonation with increasing elevation, from tropical
195 lowland forest to montane cloud forest and high-elevation ‘Puna’ grassland. The tree line lies
196 between 3,200 and 3,600 m a.s.l. For the 14 sites sampled in this study, the lower 13 sites are
197 forest and the highest site is grassland. The 14 sites are part of a network of 1 ha forest plots
198 (Nottingham et al., 2015); for each 1 ha plot, 0-10 cm surface soil was sampled from 5
199 systematically distributed locations within each 1 ha plot. Mean annual precipitation does not
200 vary significantly with altitude (mean = 2448 mm.y^{-1} , SD = 503 mm.y^{-1} ; Rapp and Silman, 2012;
201 Nottingham et al., 2015). MAAT is comprised between $26.4\text{ }^{\circ}\text{C}$ at 194 m altitude and $6.5\text{ }^{\circ}\text{C}$ at
202 3644 m altitude (Table 1). The pH is characteristic of acidic soils (3.4 - 4.7; Table 1). Further
203 information on these sites and soils is available in Nottingham et al. (2015).

204 Soil samples were collected from 10 sites between 690 m and 1,385 m a.s.l. from the
205 lake shore (20 to 50 m offshore) of 10 Andean lakes located in Chile ($38\text{--}39\text{ }^{\circ}\text{S}$) within the
206 temperate forest (Table 1). High-frequency measurements of MAAT over a period of one year
207 are available for the different sampling sites. MAAT is comprised between $5.75\text{ }^{\circ}\text{C}$ and $9.2\text{ }^{\circ}\text{C}$.
208 Soil pH ranges between 4.4 and 6.8 (Table 1).

209

210 *2.1.2. pH measurement*

211 Following sampling, soils were immediately transported to the laboratory and stored at
212 $-20\text{ }^{\circ}\text{C}$. Soil samples from the Peruvian Andes, Mt. Pollino and Mt. Shegyla were then freeze-
213 dried, ground and sieved at 2 mm. The pH of the freeze-dried samples was measured in
214 ultrapure water with a 1:2.5 soil water ratio. Typically, 10 ml of ultrapure water were added to
215 4 g of dry soil. The soil solution was stirred for 30 min, before decantation for 1 hand pH
216 measurement (Carter et al., 2007).

217

218 **2.2. Lipid analyses**

219 BrGDGTs and 3-OH FAs were analyzed in all samples from the Peruvian Andes,
220 Chilean Andes, Mt. Pollino and Mt. Shegyla.

221

222

2.2.1. 3-OH FA analysis

224 Sample preparation for 3-OH FA analysis was identical to that reported by Huguet et
225 al. (2019) and Véquaud et al. (2021). Soil samples were subjected to acid hydrolysis (3 M HCl)
226 and extracted with organic solvents. This organic fraction was then rotary-evaporated,
227 methylated in a 1M HCl-MeOH solution at 80 °C for 1 h and separated into three fractions over
228 an activated silica column: (i) 30 ml of heptane/EtOAc (98: 2), (ii) 30 ml of EtOAc and (iii) 30
229 ml of MeOH. 3-OH FAs contained in the second fraction were derivatized at 70°C for 30 min
230 with a solution of *N,O*- bis(trimethylsilyl)trifluoroacetamide (BSTFA) – Trimethylchlorosilane
231 (TMCS) 99:1 (Grace Davison Discovery Science, USA) before gas chromatography-mass
232 spectrometry (GC-MS) analysis.

3-OH FAs were analyzed with an Agilent 6890N GC-5973N using a Restek RXI-5 Sil MS silica column (60 m × 0.25 mm, i.d. 0.25 µm film thickness), as previously described (Huguet et al., 2019). 3-OH FAs were quantified by integrating the appropriate peak on the ion chromatogram and comparing the area with an internal standard (3-hydroxytetradecanoic acid, 2,2,3,4,4-d5; Sigma-Aldrich, France). The internal standard (0.5 mg/ml) was added just before injection as a proportion of 3 µl of standard to 100 µl of sample, as detailed by Huguet et al. (2019). The different 3-OH FAs were identified based on their retention time, after extraction of the characteristic *m/z* 175 fragment (*m/z* 178 for the deuterated internal standard; cf. Huguet et al., 2019).

242 The RIAN index was calculated as follows (Wang et al., 2016 ; Eq. 1) in the range
243 C₁₀-C₁₈:

$$\text{RIAN} = -\log[(I + A)/N] \quad (1)$$

245 where I, A, N represent the sum of all *iso*, *anteiso* and *normal* 3-OH FAs, respectively.

247 RAN₁₅ and RAN₁₇ indices are defined as follows (Wang et al., 2016; Eq. 2 and 3):

$$\text{RAN}_{15} = [\text{anteiso C}_{15}] / [\text{normal C}_{15}] \quad (2)$$

$$\text{RAN}_{17} = [\text{anteiso C}_{17}] / [\text{normal C}_{17}] \quad (3)$$

250 Analytical errors associated with the calculation of RIAN, RAN₁₅ and RAN₁₇ indices
251 are respectively 0.006, 0.3 and 0.2 based on the analysis of one sample injected nine times
252 during the analysis and five samples injected in triplicates.

2.2.2. *brGDGT analysis*

255 Sample preparation for brGDGT analysis was similar to that reported by Coffinet et
256 al. (2014). Briefly, ca. 5-10 g of soil was extracted using an accelerated solvent extractor (ASE)

257 100, Dionex-ThermoScientific, USA) with a dichloromethane (DCM) / methanol (MeOH)
258 mixture (9: 1) for 3×5 min at 100 °C and a pressure of 100 bars in 34 ml cells. The total lipid
259 extract was rotary evaporated and separated into two fractions of increasing polarity on a
260 column of activated alumina: (i) 30 ml of heptane: DCM (9: 1, v:v) ; (ii) 30 ml of DCM: MeOH
261 (1: 1, v:v). GDGTs are contained in the second fraction, which was rotary evaporated. An
262 aliquot (300 µL) was re-dissolved in heptane and centrifuged using an Eppendorf MiniSpin
263 centrifuge (Eppendorf AG, Hamberg, Germany) at 7000 rpm for 1 min.

264 GDGTs were then analyzed by high pressure liquid chromatography coupled with
265 mass spectrometry with an atmospheric pressure chemical ionisation source (HPLC-APCI-MS)
266 using a Shimadzu LCMS 2020. GDGT analysis was performed using two Hypersil Gold silica
267 columns in tandem (150 mm × 2.1 mm, 1.9 µm; Thermo Finnigan, USA) thermally controlled
268 at 40 °C, as described by Huguet et al. (2019). This methodology enables the separation of 5-
269 and 6-methyl brGDGTs. Semi-quantification of brGDGTs was performed by comparing the
270 integrated signal of the respective compound with the signal of a C₄₆ synthesized internal
271 standard (Huguet et al., 2006) assuming their response factors to be identical.

272 The MBT'_{5Me} index, reflecting the average number of methyl groups in 5-methyl
273 isomers of GDGTs and considered as related to MAAT, was calculated according to De Jonge
274 et al. (2014; Eq. 4):

275

$$276 \text{MBT}'_{5\text{Me}} = \frac{[\text{Ia}+\text{Ib}+\text{Ic}]}{[\text{Ia}+\text{Ib}+\text{Ic}]+[\text{IIa}+\text{IIb}+\text{IIc}]+[\text{IIIa}]} \quad (4)$$

277

278 The CBT' index, reflecting the average number of cyclopentyl rings in GDGTs and
279 considered as related to pH, was calculated as follows (De Jonge et al., 2014; Eq. 5):

280

$$281 \text{CBT}' = \log \left(\frac{[\text{Ic}]+[\text{IIa}']+[\text{IIb}']+[\text{IIc}']+[\text{IIIa}']+[\text{IIIb}']+[\text{IIIc}']}{[\text{Ia}]+[\text{IIa}]+\text{IIIa}} \right) \quad (5)$$

282

283 The Roman numerals correspond to the different GDGT structures presented in De
284 Jonge et al. (2014). The 6-methyl brGDGTs are denoted by an apostrophe after the Roman
285 numerals for their corresponding 5-methyl isomers. Analytical errors associated with the
286 calculation of MBT'_{5Me} and CBT' indices are 0.015 and 0.02 respectively, based on the analysis
287 of three samples in triplicate among the 44 soil samples.

288

289 **2.3. Statistical analysis**

290 In order to investigate the correlations between environmental variables (pH, MAAT)
291 and the relative abundances of bacterial lipids (brGDGTs and 3-OH FAs) or the indices based
292 on these compounds, pairwise correlation matrices were performed in addition to single or
293 multiple linear regressions. As the dataset is not normally distributed, Spearman correlation was
294 used with a confidence level of 5%.

295 Principal component analyses (PCA) were performed on the different soil samples to
296 statistically compare the 3-OH FA/brGDGT distributions along the different altitudinal
297 transects. The fractional abundances of the bacterial lipids (3-OH FAs and brGDGTs) were
298 used for these PCAs, with MAAT, pH and location of the sampling site representing
299 supplementary variables (i.e. not influencing the principal components of the analysis).

300 Independent models should be used for the development of environmental calibrations,
301 as each of them has its own advantages and limits. Linear regression methods are simple to use
302 but many of them suffer from the phenomenon of regression dilution, as previously noted
303 (Naafs et al., 2017; Dearing Crampton-Flood et al., 2020). That is why other models than
304 ordinary least squares or single/multiple regression were also proposed in this study (cf. section
305 4.2. for discussion of the models): the k-nearest neighbor (k-NN) and random forest models.
306 These models are based on machine-learning algorithms, which are built on a proportion of the
307 total dataset (randomly defined, i.e., training dataset) and then tested on the rest of the dataset,
308 considered as independent (test dataset).

309 The k-NN model is based on the estimation of the mean distances between the different
310 samples. This is a supervised learning method (e.g. Gangopadhyay et al., 2009). A training
311 database composed of N "input-output" pairs is initially constituted to estimate the output
312 associated with a new input x . The method of the k-neighbors takes into account the k training
313 samples whose input is the closest to the new input x , according to a distance to be defined.
314 This method is non-parametric and is used for classification and regression. In k-NN regression,
315 the result is the value for this object, which is the average of the values of the k nearest
316 neighbors. Its constraints lie in the fact that, by definition, if a range of values is more frequent
317 than the others, then it will be statistically predominant among the k closest neighbors. To
318 overcome this limitation of the k-NN method, data selection was performed randomly on the
319 dataset with a stratification modality according to the MAAT or the pH. This approach allows
320 to limit the impact of extreme values as detailed below.

322 The random forest algorithm is also a supervised learning method used, among other
323 things, for regressions (e.g. Ho, 1995; Breiman, 2001; Denisko and Hoffman, 2018;). This
324 model works by constructing a multitude of decision trees at training time and producing the
325 mean prediction of the individual trees. Decision tree learning is one of the predictive modeling
326 approaches used to move from observations to conclusions about the target value of an item.
327 Decision trees where variables are continuous values are called regression trees.

328 The training phase required for the random forests, k-NN and multiple linear
329 regression was performed on 75% of the sample set with an iteration of ten cross-validations
330 per model. Data selection was performed randomly on the dataset (with no pre-processing of
331 the individual 3-OH FAs) but with a stratification modality according to the MAAT or the pH
332 to limit the impact of extreme values on the different models used. Then, the robustness and
333 precision of the different models were tested on the remaining 25 % of samples, considered as
334 an independent dataset. Simple and Multiple linear regressions, PCA, k-NN and random forest
335 models were performed with R software, version 3.6.1 (R Core Team, 2014) using the packages
336 - tidymodels (version 0.1.0)- kknn (version 1.3.1), ranger (version 0.11.2). A web application
337 is available online (<https://athibault.shinyapps.io/paleotools>) for the reconstruction of 3-OH
338 FA-derived MAAT using the machine learning models proposed in the present study.

3. Results

3.1. Distribution of bacterial lipids

3.1.1. 3-OH FAs

343 3-OH FAs were identified in the whole dataset, representing eight elevation transects
344 and 168 samples (Supplementary table 1; Yang et al., 2015; Wang et al., 2016; Coffinet et al.,
345 2017; Huguet et al., 2019; Véquaud et al., 2021). Their chain lengths range between 8 and 26
346 C atoms, indicating that these compounds have various origins (bacteria, plants, and fungi;
347 Zelles, 1999; Wang et al., 2016 and reference therein). The homologues of 3-OH FAs with 10
348 to 18 C atoms are considered to be produced exclusively by Gram-negative bacteria
349 (Wollenweber and Rietschel, 1990; Szponar et al., 2003) and will be the only ones considered
350 in the following. Compounds with an even carbon number and *normal* chains were the most
351 abundant 3-OH FAs in all samples (mean 67.9 % of the total 3-OH FAs, Standard Deviation
352 (SD) 6.8%), with a predominance of the *n*-C₁₄ homologue (21.9%, SD 3.23%; Fig. 1). *Iso* (mean
353

354 22.9%, SD 5.01%) and *anteiso* (mean 6.33 %, SD 1.79%) isomers were also present. It must be
355 noted that *anteiso* isomers were only detected for odd carbon-numbered 3-OH FAs (Yang et
356 al., 2015; Wang et al., 2016; Coffinet et al., 2017; Huguet et al., 2019).

357 The distribution of 3-OH FAs in the soils of the different altitudinal transects did not
358 show a large variability (Fig. 1). Thus, there was no major difference in the relative abundances
359 of most of the 3-OH FAs (*i*-C₁₁, *a*-C₁₁, *n*-C₁₁, *i*-C₁₂, *a*-C₁₃, *n*-C₁₃, *i*-C₁₄, *n*-C₁₅, *i*-C₁₆, *a*-C₁₇ and
360 *n*-C₁₇) between the 8 study sites, even though slight differences could be observed for some
361 compounds as detailed below. For example, the Peruvian samples were characterized by higher
362 average proportions of *n*-C₁₈ 3-OH FA and lower contribution of the *n*-C₁₀ and *n*-C₁₂
363 homologues than those from the other transects. Soils from Mt. Shegyla were characterized by
364 lower average proportions of *n*-C₁₄ 3-OH FAs and higher abundances of *i*-C₁₇ compounds
365 compared to the other transects (Fig. 1).

366

367 3.1.2. *brGDGTs*

368 The relative abundances of brGDGTs were compared between the same transects as
369 for 3-OH FAs, representing a total of 168 samples. The 5- and 6-methyl isomers were separated
370 in most of the samples (Fig. 2, Supp. Table 2), except in older dataset, i.e. soils from Mt.
371 Rungwe (Coffinet et al., 2014, 2017). BrGDGT data from Mt. Rungwe will not be further
372 considered in this study.

373 The brGDGT distribution was dominated by acyclic compounds (Ia, IIa, IIa', IIIa,
374 IIIa') which represent on average ca. 83.4% of total brGDGTs (SD = 14.5%; Fig. 2). The
375 tetramethylated (Ia-c; mean 39.3%, SD of 20.5%) and the pentamethylated (IIa-c; 44.8%, SD
376 12.8%) brGDGTs were predominant over the hexamethylated ones (IIIa-c; Fig. 2). The 5-
377 methyl isomers were on average present in a higher proportion (mean 71.9%, SD 23.4%) than
378 the 6-methyl compounds (Fig. 2).

379 High variability of the brGDGT distribution was observed among the different
380 transects. The relative abundance of brGDGT Ia was much higher in the Peruvian soils (mean
381 83%, SD 12.6%) than in the other transects (mean between 17.3% and 61.7%; Fig. 2). The 5-
382 methyl isomers were more abundant than the 6-methyl isomers for all sites except for Mt.
383 Pollino (mean 5-methyl = 44%, SD=11.7%) and Mt. Majella (mean 5-methyl = 33.7 %, SD =
384 5.5%; Fig. 2).

385

386 **3.2. 3-OH FA and brGDGT-derived indices**387 **3.2.1. 3-OH FA**

388 The RIAN index varied between 0.1 and 0.8 among the eight elevation transects (Table
389 1). The RIAN index ranged from 0.37 to 0.67 for the Peruvian Andes, 0.23 to 0.56 for Mt.
390 Shegyla, 0.15 to 0.34 for Mt. Pollino, 0.21 to 0.53 for the Chilean Andes, 0.26 to 0.80 for Mt.
391 Rungwe (Huguet et al., 2019), 0.16 to 0.46 for Mt. Majella (Huguet et al., 2019), 0.20 to 0.69
392 for Mt. Shennongjia (Wang et al., 2016) and 0.13 to 0.56 for the French Alps (Véquaud et al.,
393 2021).

394 The RAN₁₅ varied greatly among the different sites (Table 1). It was in the same range
395 along Mts. Rungwe (1.04-5.73) and Majella (0.68-6.43; Huguet et al., 2019). In contrast, its
396 upper limit was higher for Mts. Shennongjia (0.68-10.18; Wang et al., 2016), Shegyla (4.07-
397 12.17), Pollino (2.41-10.26), the Peruvian Andes (2.45-13.77) and the French Alps (1.44-
398 12.26). The range of variation in RAN₁₅ was narrower for the Chilean Andes (3.82-6.40).

399 The RAN₁₇ values were similar among the different altitudinal transects (Table 1),
400 ranging from 1.72 to 3.90 along Mt. Shegyla, 0.73 to 4.75 along Mt. Majella (Huguet et al.,
401 2019), 1.19 to 4.54 along Mt. Pollino, 1.91 to 4.25 for the Chilean Andes and 1.12 to 3.57 along
402 Mt. Shennongjia (Wang et al., 2016). The range of RAN₁₇ values was narrower for Mt. Rungwe
403 (0.33-1.62; Huguet et al., 2019) and the Peruvian Andes (0.61-2.39) and wider for the French
404 Alps (0.89-6.42; Véquaud et al., 2021) compared to the other sites.

405

406 **3.2.2. brGDGT**

407 The range of variation in the MBT'_{5Me} index was homogeneous along most transects
408 (0.32-0.63; Table 1), except the Peruvian Andes, with higher values (0.58-0.98; Table 1).
409 Regarding the CBT' index, it showed similar ranges along Chilean Andes (-2.28 to -0.32) and
410 Mt. Shegyla (-2.39 to -0.35; Table 1). This index showed different ranges of variations along
411 the other altitudinal transects, Mts. Shennongjia (-1.18 to 0.50; Yang et al., 2015), Pollino (-
412 0.24 to 0.43) and Peruvian Andes (-1.91 to -1.09). Finally, The CBT' values varied within a
413 narrow range along Mt. Majella (0.23-0.59; Huguet et al., 2019) and within a wide range along
414 the French Alps (-2.29 to 0.52 ; Véquaud et al., 2021).

415

416 **3.3. Principal component analysis and clustering of 3-OH FA and brGDGT**
417 **distribution**

418 Principal component analyses were performed to refine the comparison of bacterial
419 lipid distribution (3-OH FAs and brGDGTs) among the different altitudinal transects.

421 **3.3.1. 3-OH FA**

422 The first two axes of the 3-OH FA PCA explained 39.1% of the total variance in the
423 dataset (Fig. 3a). Dimension 1 (23.9%) opposed samples from Mt. Pollino in the right quadrant
424 to Peruvian soils and samples from Mt. Shennongjia. Dimension 2 (15.2%) especially separated
425 individuals from Chile and Mt. Rungwe. The Wilks' test showed that the location of the
426 sampling sites was the best variable discriminating the distribution of the individuals in the
427 PCA.

428 Principal component analysis performed on the temperature (RAN₁₅, RAN₁₇) and pH
429 (RIAN) indices derived from 3-OH FAs showed that most of the variance was carried by the
430 first two axes of the PCA (Axis 1 = 56.09%; Axis 2 = 35.29%; Supp. Fig. 2). The first axis was
431 highly correlated with the RAN₁₅ ($r = 0.87$) and RAN₁₇ ($r = 0.93$) as well as with MAAT ($r =$
432 0.67), while Axis 2 showed strong correlations with the RIAN ($r = 0.96$) and pH ($r = -0.61$).
433 The PCA allowed visualizing relationships at the scale of the whole dataset, between MAAT
434 and RAN₁₅ and RAN₁₇ ($r = -0.61$; $r = -0.64$ respectively) and between pH and RIAN ($r = -0.53$).
435

436 **3.3.2. brGDGT**

437 The first two axes of the brGDGT PCA explained 57.7% of the total variance in the
438 dataset (Fig. 3b). Dimension 1 (42.6%) strongly discriminated soils from Mt. Majella and, to a
439 lesser extent, Mt. Pollino, in the right quadrant from those from Mt. Shegyla, Peruvian Andes
440 and Chilean Andes in the left quadrant. Mts Majella and Pollino were also discriminated
441 negatively along dimension 2 (15.1%). Samples from Mts. Shennongjia and Lautaret-Galibier
442 were distributed over the entire PCA. As for the 3-OH FAs, Wilks' test showed that the location
443 of the sampling sites was the best variable discriminating the distribution of the brGDGTs in
444 the PCA.

446

4. Discussion

447 4.1. 3-OH FA and brGDGT-derived proxies

448 Previous studies conducted on soils from individual altitudinal transects revealed (1)
449 local linear relationships between MAAT/pH and 3-OH FA indices and (2) the potential for
450 combined calibrations using simple linear regressions (Wang et al., 2016; Huguet et al., 2019;
451 Véquaud et al., 2021). In the present study, the existence of linear relationships between 3-OH
452 FA-derived indices and environmental variables was further investigated using an extended soil
453 dataset and the corresponding results were compared with those derived from the brGDGTs,
454 used as an established reference proxy.

455

456 4.1.1. Relationships between pH and bacterial lipid-derived proxies

457 The relationship between RIAN and pH was investigated along each of the altitudinal
458 transects (Fig. 4a; Supp. Table 3). No significant linear relationship was obtained for the
459 Peruvian Andes, Mts. Rungwe, Pollino and Majella (Huguet et al., 2019) and weak to moderate
460 correlations were observed along Mts. Shegyla and Lautaret-Bauges ($R^2 = 0.29-0.46$; Supp.
461 Table 3). In contrast, strong regressions between RIAN and pH were observed along Mt.
462 Shennongjia ($R^2 = 0.71$) and in Chilean Andes ($R^2 = 0.66$). A weak linear relationship between
463 RIAN and pH ($R^2=0.34$; RMSE = 0.99; $p = 7.39 \times 10^{-17}$) was also obtained when considering
464 the 168 samples for the eight elevation transects altogether. Therefore, our results confirm the
465 general influence of pH on the relative abundance of 3-OH FAs (Huguet et al., 2019) but
466 suggest that strong linear correlations between RIAN and pH can only be obtained (i) at a local
467 level and (ii) only for some of the sites.

468 As previously suggested (Huguet et al., 2019), the absence or weakness of linear
469 correlations between RIAN and pH may be at least partly due to the small range of variation of
470 pH (<2 units) along some mountains, such as Mts. Rungwe, Majella, and the Peruvian Andes
471 (Fig. 4a; Table 1, Huguet et al., 2019). Transects for the Peruvian Andes and Mt. Majella were
472 also characterized by the absence of relationships between pH and the brGDGT-derived CBT'
473 index, supporting the hypothesis that narrow pH ranges limit the potential of obtaining linear
474 relationships between indices based on bacterial lipids and pH. Nevertheless, the existence of a
475 narrow pH range was not the only limiting factor in obtaining a strong linear regression between
476 RIAN and pH. Indeed, MAAT rather than soil pH was the dominant driver of soil bacterial
477 diversity and community composition for the Peruvian transect (determined using 16S rRNA
478 sequencing (Nottingham et al., 2018) and phospholipid fatty acids (Whitaker et al., 2014)),

479 consistent with the weak correlation between soil pH and bacterial lipids. The weakness of the
480 RIAN-pH relationship may also be partly due to the heterogeneity of soils encountered along a
481 given altitudinal transect, representing specific microenvironments and to the large diversity of
482 bacterial communities in soils from different elevations (Siles and Margesin, 2016). The
483 distribution of 3-OH FAs varies greatly among Gram-negative bacterial species (Bhat and
484 Carlson, 1992) which may account for the significant variability in RIAN values observed in
485 soils from a given transect. Altogether, these results suggest that linear models are not the most
486 suitable for establishing a global calibration between RIAN and pH in soils.

487 Concerning GDGTs, moderate to strong relationships between brGDGT-derived CBT'
488 index and pH were observed along 5 of the 7 altitudinal transects investigated (Fig. 4b; Supp.
489 Table 3). All the individual linear relationships between CBT' and pH, where present, had
490 similar slopes and ordinates and share (for most of the samples) the same 95% confidence
491 intervals (p -value <0.5). This resulted in a strong linear relationship between CBT' index and
492 pH values for the dataset ($R^2 = 0.68$; RMSE = 0.71; $n = 140$), which is weaker than the global
493 calibration ($R^2 = 0.85$; RMSE = 0.52; $n = 221$) proposed by De Jonge et al. (2014).

494 The discrepancy in relationships between temperature and brGDGTs and 3-OH FAs
495 might partly be due to differences in the relative abundance of these lipids among bacterial
496 communities. The brGDGTs are produced by a more restricted and less diverse number of
497 bacterial species than 3-OH FAs, which are arguably biosynthesized by a large diversity of
498 Gram-negative bacteria species (e.g. Wakeham et al., 2003, Zelles et al., 1995; Zelles, 1999).
499 So far, only bacteria from the *Acidobacteria* phylum were identified as putative brGDGT
500 producers in soils (Sinninghe Damsté et al., 2018). The hypothetical lower diversity of brGDGT
501 producers, in contrast with 3-OH FAs, might explain the more homogenous response and lower
502 scatter of the relationships between pH and CBT' index. Moreover, the CBT' index is a ratio
503 based on a restricted number of compounds, representing the direct dependence of the degree
504 of cyclisation of bacterial GDGTs on pH. Conversely, the RIAN index is calculated from the
505 relative abundances of all the individual 3-OH FAs between C₁₀ and C₁₈ (Wang et al., 2016). It
506 cannot be ruled out that some of the compounds used to calculate the RIAN index are
507 preferentially synthesized, as part of the homeoviscous mechanism, in response to
508 environmental variables other than pH. This calls for a better understanding of the ecology of
509 3-OH FA-producing bacteria and their adaptation mechanisms.

510

511 4.1.2 Relationships between MAAT and bacterial lipid-derived proxies

512 RAN₁₅ was previously shown to be correlated with MAAT along Mts. Rungwe,
513 Majella and Shennongjia (Wang et al., 2016; Huguet et al., 2019). Moderate to strong linear
514 correlations ($R^2 = 0.49-0.79$) between RAN₁₅ and MAAT were also observed along most of the
515 individual transects investigated (Fig. 5a; Supp. Table 3, except along the Chilean and Lautaret-
516 Bauges transects. The individual correlations do not share the same 95% confidence intervals
517 and even when some of them present similar slopes, the regression lines display significantly
518 different intercepts (p -value > 0.05) (Fig. 5a). This supports the hypothesis of a site-dependent
519 effect of the linear RAN₁₅-MAAT relationship previously made by Huguet et al. (2019).

520 Similarly, to RAN₁₅, RAN₁₇ was moderately to strongly correlated ($R^2 = 0.53-0.81$)
521 with MAAT along 5 out of 8 individual transects (Fig. 5b; Supp. Table 3). The small range of
522 variation in MAAT along the Chilean transect (6.0-9.2 °C) (Table 1), associated with that of
523 the RAN₁₅/RAN₁₇, could explain the lack of a linear relationship between the MAAT and these
524 indices. As for the French Alps (Mts Lautaret-Bauges), the influence of local environmental
525 parameters (pH and to a lesser extent soil moisture and grain size, related to vegetation and soil
526 types, or thermal regimes associated with the snow cover) on 3-OH FA distribution was shown
527 to be predominant over that of MAAT (Véquaud et al., 2021). In contrast with RAN₁₅, the linear
528 regressions between RAN₁₇ and MAAT along Mts. Shegyla, Shennongjia, Rungwe and the
529 Peruvian Andes transects share confidence intervals at 95% and have similar slope and intercept
530 values (p -value < 0.05 ; Fig. 5b; Supp. Table 3), suggesting that RAN₁₇ could be a more effective
531 global proxy for MAAT reconstructions than RAN₁₅.

532 In order to test the hypothesis that RAN₁₇, rather than RAN₁₅, is a more effective
533 global proxy for MAAT, the global calibrations between RAN₁₅/RAN₁₇ and MAAT based on
534 the entire soil dataset ($n = 168$) were compared. The two linear regressions had similar moderate
535 determination coefficients ($R^2 = 0.37$ and 0.41 for RAN₁₅ and RAN₁₇, respectively) and similar
536 high RMSE (RMSE = 5.46°C and 5.28°C for RAN₁₅ and RAN₁₇, respectively; Supp. Table 3).
537 For all transects (except for the Mt Majella RAN₁₇/MAAT relationship), the individual local
538 regressions between RAN₁₅/RAN₁₇ and MAAT outperformed the proposed global linear
539 calibrations in terms of determination coefficients (0.49-0.81) and RMSE (1.98-3.57 °C; Supp.
540 Table 3), suggesting that local rather than global linear transfer functions based on RAN₁₅ or
541 RAN₁₇ may be more appropriate for paleotemperature reconstructions in soils.

542 The difficulties in establishing global linear RAN₁₅/RAN₁₇-MAAT calibrations may
543 partly be due to the fact that microbial diversity, especially for 3-OH FA-producing Gram-
544 negative bacteria (Margesin et al., 2009; Siles and Margesin, 2016), can vary greatly from one

545 soil to another, resulting in variation of the RAN₁₅/RAN₁₇ indices, as also assumed for the
546 RIAN. The strong regional dependence of the 3-OH FA distribution may thus explain the weak
547 correlation between 3-OH FA-derived indices (RAN₁₅, RAN₁₇ and RIAN) and environmental
548 variables (MAAT/pH) at a global level. This regional dependency was further supported by the
549 PCA of the relative abundance of 3-OH FAs across the global dataset, which showed that the
550 individuals were grouped based on the sampling location (Fig. 3a).

551 In addition to 3-OH FAs, the relationships between brGDGT distribution and MAAT
552 were investigated along the seven transects for which the 5- and 6-methyl brGDGT isomers
553 were separated (Mts Shegyla, Pollino Majella, Lautaret-Bauges, Shennongjia, Peruvian Andes
554 and Chilean Andes). These individual transects showed moderate to strong relationships
555 between MAAT and MBT'_{5Me} (R^2 0.35-0.89; Fig. 6 and Supp. Table 3), with similar slopes and
556 ordinates (except for the Peruvian Andes) and shared 95% confidence intervals for most of the
557 samples. A distinct relationship between MBT'_{5Me} and MAAT was observed along the Peruvian
558 Andes and Mt Majella transects (Fig. 6a), as also observed for the RIAN and RAN₁₅ indices
559 (Figs 4a and 5a). The singularity of the Peruvian soils is also visible on the PCA performed on
560 the brGDGT distribution (Fig. 3b), where the samples from this region are pooled separately
561 from the rest of the dataset. This specific trend is difficult to explain, even though the Peruvian
562 Andes are subjected to warmer climatic conditions (Table 1) than the other temperate transects,
563 which may in turn affect the nature of the microbial communities encountered in the soils and
564 the bacteria lipid distribution (Siles and Margesin, 2016; Hofmann et al., 2016; De Jonge et al.,
565 2019).

566 A moderate linear relationship between MAAT and MBT'_{5Me} ($MAAT = 24.5 \times MBT'^{5Me}$
567 -4.78; $R^2 = 0.57$, RMSE = 3.39 °C, $n = 140$; Supp. Table 3) was observed after combining the
568 data for the seven aforementioned altitudinal transects. This global relationship follows a
569 similar trend as the calibration proposed by De Jonge et al. 2014 ($MAAT = 31.45 \times MBT'^{5Me}$ -
570 8.57) and is more robust and accurate than those obtained between the RAN₁₅/RAN₁₇ and
571 MAAT (Supp. Table 3). This confirms that the MBT'_{5Me} index can be applied at a global scale
572 using a simple linear regression model as previously shown (De Jonge et al., 2014; Naafs et al.,
573 2017), in contrast with the RAN₁₅ and RAN₁₇ proxies, for which only strong local calibrations
574 with MAAT were found.

575 As a similar conclusion was obtained for the RIAN-pH proxy, it appears necessary to use
576 more complex models to develop global calibrations between 3-OH FA-derived proxies and
577 MAAT/pH. This novel method allows taking into account the complexity and specificity of
578 each environmental site.

579 **4.2. Development of new models for the reconstruction of MAAT and pH from 3-**
580 **OH FA**

581 Several complementary methods were recently used to derive calibrations with
582 environmental parameters from organic proxies. Most calibrations between lipid distribution
583 and environmental variables were based on simple linear regression models, most often the
584 ordinary least square regression (e.g. for brGDGTs: De Jonge et al., 2014; Wang et al., 2016),
585 as it is simple and easy to implement and understand. Other linear models, such as Deming
586 regression (Naafs et al., 2017) or Bayesian regression (Tierney and Tingley, 2014; Dearing
587 Crampton-Flood et al., 2020) were also used. Nevertheless, these single linear regression
588 methods rely on a given index (e.g. MBT'_{5Me} or CBT' for brGDGTs) which is correlated with
589 environmental parameters. This represents a limitation, as the relative distribution of bacterial
590 lipids can be concomitantly influenced by several environmental parameters (e.g. Véquaud et
591 al., 2021) and can also depend on the diversity of the bacteria producing these compounds
592 (Parker et al., 1982; Bhat and Carlson, 1992; Zelles, 1999). In contrast, using bacterial lipid
593 relative abundances rather than a single index in the relationships with environmental variables
594 appears less restrictive, and more representative of the environmental complexity. Other models
595 can be used in this way, such as those based on multiple regressions (e.g. Peterse et al., 2012;
596 De Jonge et al., 2014; Russell et al., 2018), describing the relationships between one or several
597 explained variables (e.g. bacterial lipid abundances) and one or several explanatory variables
598 (e.g. MAAT, pH). Multiple regressions can reveal the presence of linear relationships among
599 several known variables but cannot take into account non-linear influences, which may occur
600 in complex environmental settings. This limitation, common to all linear models, can be
601 overcome using non-parametric methods such as some of the machine-learning algorithms (e.g.
602 nearest neighbours or random forest; Dunkley Jones et al., 2020). The reliability of the latter
603 models lies in the fact that they are non-linear, which helps capturing the intrinsic complexity
604 of the environmental setting, and that they avoid the regression dilution phenomenon observed
605 in most linear models. Moreover, their robustness is improved by the fact that they are built on
606 a randomly defined proportion of the total dataset and then tested on the rest of the dataset,
607 considered as independent. Last, these machine-learning algorithms are flexible and are
608 continuously evolving when adding new samples.

609 As shown in section 4.1., robust global calibrations between 3-OH FA-derived indices
610 (RIAN, RAN₁₅ and RAN₁₇) and MAAT/pH could not be established using a simple linear
611 regression model, contrary to what was observed with brGDGT-derived indices. Therefore,

612 three different independent and complementary models were tested to potentially establish
613 stronger statistical relationships between 3-OH FA distributions and pH/MAAT at the global
614 level : (i) a parametric model – multiple linear regression; (ii) two non-parametric models –
615 random forest (e.g. Ho, 1995; Denisko and Hoffman, 2018) and k-NN algorithms (e.g.
616 Gangopadhyay et al., 2009). As discussed above, the multiple linear regression model allows
617 the determination of linear relationships between MAAT/pH and the individual relative
618 abundances of 3-OH FAs, instead of indices derived from the latter. As for the two non-
619 parametric models, they present among other things the advantage of taking into account non-
620 linear environmental influences.

621 The three models, based on a supervised machine learning approach, were applied to
622 the total soil dataset ($n=168$). All the 3-OH FA homologues of Gram-negative bacterial origin
623 (i.e. with chain lengths between C₁₀ and C₁₈; Wilkinson et al., 1988) were included in the models
624 whatever their abundance to keep the maximum variability and take into account the specificity
625 and complexity of each altitudinal transect. Indeed, the nature of the individual 3-OH FAs
626 whose fractional abundance is mainly influenced by MAAT/pH may be site-dependent, as
627 previously observed (Véquaud et al., 2021). The performances of these three models were
628 compared with those of the linear calibrations between 3-OH FA-derived indices (RAN₁₅,
629 RAN₁₇, RIAN) and MAAT/pH (Table 2).

630

631 *4.2.1. Temperature calibrations*

632 The multiple linear regression model yielded a strong relationship between 3-OH FA
633 relative abundances and MAAT (Fig. 7a; Eq.6):

$$634 MAAT(^{\circ}C) = -59.02 \times [nC_{10}] + 102.1 \times [iC_{11}] + 2628.49 \times [aC_{11}] - 165.58 \times [nC_{11}] - 79.799 \\ 635 \times [nC_{12}] + 89.93 \times [iC_{13}] + 205.06 \times [aC_{13}] - 136.25 \times [nC_{13}] - 309.71 \times [iC_{14}] - 43.16 \times \\ 636 [nC_{14}] - 9.27 \times [iC_{15}] - 308.53 \times [aC_{15}] + 66.06 \times [nC_{15}] - 60.57 \times [iC_{16}] + 15.53 \times [nC_{16}] + \\ 637 13.52 \times [iC_{17}] - 228.76 \times [aC_{17}] - 91.12 \times [nC_{17}] + 43.71 \\ 638 (n = 168; R^2 = 0.79; RMSE = 3.0 ^{\circ}C) \quad (6)$$

639 This model, which takes into account the Gram-negative bacterial 3-OH FAs (C₁₀-C₁₈;
640 Wilkinson et al., 1988), presents a higher strength than the global linear relationships between
641 3-OH FA derived indices and MAAT (R²=0.37 and 0.41; RMSE =5.5°C and 5.3°C for RAN₁₅
642 and RAN₁₇, respectively; Table 2). The multiple linear regression also improves the accuracy
643 and robustness of MAAT prediction in comparison with single linear relationships, with lower
644 RMSE (3.0 °C), variance of the residuals (9.2 °C; Fig. 7d) and mean absolute error (MAE; 2.3

645 °C) than with the RAN₁₅ and RAN₁₇ calibrations (RMSE of 5.5 and 5.3 °C; variance of 29.8
646 and 27.9 °C; MAE of 4.0 and 3.9 °C for RAN₁₅ and RAN₁₇, respectively; Table 2).

647 Similarly to the multiple linear regression model (Fig. 7a), the random forest (Fig. 7b)
648 and k-NN (Fig. 7c) calibrations are characterized by strong determination coefficients (R^2 0.83
649 and 0.77, respectively). The variance in residuals, MAE and RMSE of the random forest
650 calibration are slightly lower than those of the multiple linear regression and k-NN models
651 (Table 2). An advantage of the random forest algorithm lies in the fact that the weight of the
652 different variables used to define the model can be quantified using the permutation importance
653 method (Breiman, 2001). The *a*-C₁₅, *i*-C₁₄, *a*-C₁₇, *n*-C₁₂, *n*-C₁₅, and to a lesser extent *n*-C₁₇, *n*-
654 C₁₆ and *i*-C₁₃ 3-OH FAs were observed to be the homologues predominantly used by the model
655 to estimate MAAT values (Fig. 9a). They include all the 3-OH FAs involved in the calculation
656 of the RAN₁₅ and RAN₁₇ indices, especially the *a*-C₁₅ homologue. This may explain why linear
657 relationships between the RAN₁₅/RAN₁₇, and MAAT could be established along some, but not
658 all, of the altitudinal transects investigated until now (Wang et al., 2016; Huguet et al., 2019;
659 Véquaud et al., 2021; this study). Nevertheless, other individual 3-OH FAs than those appearing
660 in the calculation of the RAN₁₅ and RAN₁₇ have also a major weight in the random forest model
661 and seem to be influenced by temperature changes, explaining the moderate determination
662 coefficients of the global RAN₁₅/RAN₁₇-MAAT linear relationships observed in this study.

663 On the whole, the strength and accuracy of the multiple linear regression, k-NN and
664 random forest models are much higher than those based on the RAN₁₅ and RAN₁₇ indices
665 (Table 2). This is likely related to the fact that the three aforementioned models integrate the
666 whole suite of 3-OH FAs homologues (C₁₀ to C₁₈) and thus better capture the complexity of the
667 response of soil Gram-negative bacteria and their lipid distribution to temperature changes than
668 the RAN₁₅ and RAN₁₇ indices. They also present the advantage of increasing the range of
669 temperature which may be predicted by more than 4 °C in comparison with the RAN₁₅ and
670 RAN₁₇ calibrations (Table 2). Indeed, even though the lower limit of MAAT estimates for the
671 three models tested in the present study is slightly higher than those based on the RAN₁₅ and
672 RAN₁₇ indices, the upper limit of the MAAT which can be estimated using the multiple linear
673 regression, random forest and k-NN models is substantially higher (ca. 25 °C) than that based
674 on the RAN₁₅ or RAN₁₇ indices (ca. 17 °C; Table 2).

675 The three proposed models show the potential of 3-OH FAs as MAAT proxies at the
676 global level, which was not visible using RAN₁₅ and RAN₁₇ indices. The non-parametric
677 models (random forest and k-NN) may benefit from the fact that they take into account the
678 complex, non-linear relationships between environmental parameters and bacterial lipid

679 abundance. This is highlighted when comparing the independent variations of the individual 3-
680 OH FA relative abundances with estimated MAAT for the three proposed models, with non-
681 linear trends for the k-NN and random forest models, in contrast with the multiple linear
682 regression (Supp. Fig. 2).

683

684 4.2.2. *pH calibrations*

685 A robust linear relationship between the RIAN and pH could not be obtained from the
686 whole soil dataset (Fig. 4a; Table 2). In contrast, the multiple regression model provided a
687 strong correlation between the 3-OH FA fractional abundances and pH (Fig. 8a; Eq. 7):

$$688 \text{pH} = -1.45 \times [nC_{10}] - 31.70 \times [iC_{11}] - 162.09 \times [aC_{11}] - 53.22 \times [nC_{11}] - 6.21 \times [nC_{12}] + \\ 689 56.24 \times [iC_{13}] - 2.02 \times [aC_{13}] + 15.10 \times [nC_{13}] + 23.99 \times [iC_{14}] - 4.54 \times [nC_{14}] - 13.79 \times \\ 690 [iC_{15}] - 15.74 \times [aC_{15}] + 1.93 \times [nC_{15}] - 46.29 \times [iC_{16}] - 3.20 \times [nC_{16}] - 1.80 \times [iC_{17}] - \\ 691 8.90 \times [aC_{17}] + 11.46 \times [nC_{17}] - 3.63 \times [nC_{18}] + 7.84 \quad (n = 168; R^2 = 0.64; \text{RMSE} = 0.8) \quad (7)$$

692 The random forest (Fig. 8b) and k-NN pH models (Fig. 8c) appeared to be slightly more
693 robust and accurate than the multiple linear regression (Fig. 8a), as the former two models
694 presented slightly higher determination coefficients ($R^2 = 0.68$ and 0.70 for k-NN and random
695 forest, respectively) and slightly lower RMSE (0.7), variance in residuals (0.5) and MAE (0.5)
696 than the multiple linear regression (Table 2).

697 As for the MAAT random forest model, the weight of the individual 3-OH FAs in the pH
698 random forest calibration was determined (Fig. 9b). Three homologues – *i*-C₁₃, *n*-C₁₅, *i*-C₁₆ –
699 had a larger weight in the global pH model than the others (Fig. 9b). This is consistent with a
700 detailed study of 3-OH FA distribution in soils from the French Alps (Véquaud et al., 2021),
701 where the *i*-C₁₃ and *i*-C₁₆ 3-OH FAs were observed to be predominantly influenced by pH.
702 Nevertheless, in addition to the three aforementioned homologues, most of the C₁₀ to C₁₈ 3-OH
703 FAs have a non-negligible influence in the random forest pH model, except the *a*-C₁₅ and *i*-C₁₄
704 compounds (Fig. 9b). This is in line with the definition of the 3-OH FA-based pH index (RIAN)
705 defined by Wang et al. (2016) which includes the whole suite of 3-OH FAs. These results
706 suggest that soil Gram-negative bacteria may respond to pH variations by modifying the whole
707 distribution of associated 3-OH FAs (C₁₀-C₁₈). This would need to be further confirmed by e.g.
708 investigating the influence of pH variations on pure strains of Gram-negative bacteria isolated
709 from soils.

710 In any case, in contrast with the RIAN index, the multiple linear regression, k-NN and
711 random forest models provided strong global calibrations with pH (Fig. 8), as robust as the
712 global CBT'-pH relationship (Fig. 4b). The three proposed models also increase the range of

pH which can be estimated (~ 4 pH units) in comparison with the RIAN global calibration (~ 3 pH units), further strengthening the potential of these models for soil pH reconstruction. As MAAT models, the independent variations of the individual 3-OH FA relative abundances with estimated pH highlight non-linear trends for the k-NN and random forest models, in contrast with the multiple linear regression (Supp. Fig. 3), which might favor the use of the two non-parametric models in order to take into account such non-linear influences. The machine-learning MAAT and pH models proposed in this paper are flexible and could be further improved by increasing the number of soil samples analyzed and the representativeness of the different MAAT and pH values within the dataset.

722

723 **4.3. Paleoclimate application of the new 3-OH FA/MAAT models**

724

725 The multiple regression, random forest and k-NN models developed for MAAT
726 reconstruction using 3-OH FAs were similar in terms of robustness and precision (Figs. 7a, b,
727 c; Table 2). The performance and validity of these global terrestrial calibrations for
728 paleotemperature reconstructions were thus tested and compared with the MAAT record from
729 a Chinese speleothem (HS4 stalagmite) covering the last 9,000 years BP (Wang et al., 2018).
730 This terrestrial archive was the object of previous paleostudies, thus providing a context for the
731 interpretation of the MAAT data and, to the best of our knowledge, represents the only
732 published application of 3-OH FAs as a paleotemperature proxy in terrestrial settings (Wang et
733 al., 2018). The local comparison of 3-OH FA distributions in the overlying soils and stalagmites
734 and the analyses of bacterial diversity and transport pathways suggested that the 3-OH FAs in
735 the HS4 speleothem were mainly soil-derived (Wang et al., 2018), supporting the application
736 of soil calibrations for MAAT reconstruction from this archive, although not being a paleosoil
737 itself. The first paleoapplication of 3-OH FAs (Wang et al., 2018) on this speleothem relied on
738 a local calibration between the RAN₁₅ index and MAAT proposed by Wang et al. (2016) using
739 soils from Mt. Shennogjia. The MAAT estimates derived from our global soil calibrations were
740 compared with those obtained from this local soil calibration (Wang et al., 2016).

741

742

743 *4.3.1 Comparison of the multiple linear regression, k-NN and random forest global 744 MAAT calibrations*

745 The multiple regression model (Eq. 6; Fig. 7a) yielded MAAT estimates ranging
746 between -35 and 22.8 °C over the last 9,000 years (Supp. Fig. 4). The temperature minimum (-

747 35°C) observed at 560 yrs BP can be considered as an outlier, with a significantly lower MAAT
748 estimate than those provided by the other samples. After having ignored this apparent outlier,
749 the MAAT range over the last 9,000 years was comprised between 3.2°C and 22.8°C, with
750 temperature shifts of up to 15 °C within very short periods of time. The observed range of
751 MAAT and large variations in temperature over such short periods appear far too excessive, as
752 the expected amplitude of MAAT during the Holocene is expected to be up to ca. 2-3 °C (Liu
753 et al., 2014). This highly questions the reliability of the multiple linear regression model for
754 MAAT reconstruction from this archive.

755 MAAT estimates derived from the k-NN calibration ranged between 6.5 and 19.7 °C
756 over the last 9,000 years (Supp. Fig. 4). Abrupt shifts in MAAT of more than 10 °C were
757 observed between 2,000 and 4,000 yrs BP. Such variations, higher than the RMSE of the
758 calibration, appear excessive for the Holocene period, as previously discussed for the multiple
759 regression model. The bias in MAAT estimates may be due to the intrinsic definition of the k-
760 NN model, which is better suited for uniformly distributed datasets. This is not the case here,
761 as the individual transects heterogeneously cover a wide range of temperatures. The application
762 of a global calibration at the local scale – that of the HS4 stalagmite – using the k-NN method
763 and based on the similarities among samples, thus does not appear appropriate. Such a
764 calibration might be improved by extending the dataset with samples more equally distributed
765 across a wider range of global climatic gradients.

766 Finally, the random forest model yielded MAAT estimates between 10.6 and 19.3°C,
767 i.e. a smaller estimation range than the k-NN algorithm and multiple regression model (Supp.
768 Fig. 4). The amplitude of the shifts observed between 2,000 and 4,000 yrs BP was ca. 4°C,
769 which is climatically more consistent than the variations obtained with the k-NN method and
770 multiple regression model, even though these large variations in MAAT over such short periods
771 of time still appear too excessive. Furthermore, the application of the global random forest
772 calibration roughly provided similar temperature trends as those derived from the local RAN₁₅
773 calibration by Wang et al. (2018; Fig. 10), despite some largest oscillations for the global model.
774 These results suggest that the random forest calibration is more reliable than the multiple
775 regression and k-NN ones. This can be explained by the intrinsic definition of the random forest
776 algorithm, which averages the results of several independent models (so-called decision trees),
777 thus reducing the variance and thus the forecast error on the final model. This is also in line
778 with the slightly higher accuracy of the random forest calibration compared with the other two
779 models (Table 2), as previously discussed. In contrast, the multiple regression calibration was
780 the less performant of the three models on the investigated archive. This may be related to its

781 parametric nature and the fact that it does not take into account the natural non-linear variations
782 on 3-OH FA fractional abundances highlighted by the random forest and k-NN models (Supp.
783 Figs. 2 and 3).

784 In conclusion, the three models proposed in this study, especially the random forest,
785 have potential for MAAT reconstruction, even though the application to a well-known
786 paleoclimate archive showed their limitations. This highlights the importance of testing new
787 calibrations on well-characterized archives to investigate their reliability.

788

789 *4.3.2. Comparison of the global random forest and local RAN₁₅ calibrations for MAAT
790 reconstruction*

791 The random forest model was observed to be the most reliable of the three proposed
792 global MAAT calibrations (Fig. 7). To go further, we compared the temperature record derived
793 from our global random forest calibration with that derived from the local MAAT/RAN₁₅
794 transfer function proposed by Wang et al. (2016; Fig. 10). The application of the local RAN₁₅
795 calibration to the HS4 stalagmite yielded an average MAAT of ca. 18.4 °C over the most recent
796 part of the record (last 800 yrs; Fig. 10), consistent with the MAAT of 18 °C recorded *in situ*
797 by a temperature logger (Hu et al., 2008; Wang et al., 2018). In contrast, absolute MAAT
798 estimates derived from the random forest model were on average 14.2 °C over the last 800 yrs
799 and were generally lower than those obtained from the local RAN₁₅ calibration over the whole
800 record. Altogether, these results suggest that the random forest model tends to underestimate
801 absolute MAAT, in contrast with the RAN₁₅ calibration proposed by Wang et al. (2016). This
802 discrepancy may be due the fact that the calibration proposed in the present study is based on a
803 global dataset, with samples subject to a large variety of environmental and climatic conditions,
804 whereas the RAN₁₅-MAAT transfer function by Wang et al. (2016) was constructed using soil
805 samples from a regional altitudinal transect, located at only 120 km distance from the stalagmite
806 site (Wang et al., 2018).

807 Even though the local calibration by Wang et al. (2016) provides more accurate
808 absolute MAAT values than the present global random forest model, as it could be expected,
809 both calibrations roughly generate similar qualitative MAAT trends over time. A regular slight
810 decrease in temperature of ca. 1 °C was observed between 9,000 and ca. 1,000 yrs BP based on
811 the local RAN₁₅ calibration (Fig. 10a; Wang et al., 2018). This general decreasing trend was
812 also visible when using the random forest model, but with larger oscillations and mainly
813 between 9,000 and 4,000 yrs BP, in agreement with the general trend recorded by the $\delta^{18}\text{O}$
814 record (mixture of temperature and hydrological signals, Wang et al., 2018) of the HS4

815 stalagmite (Fig. 10b,c; Hu et al., 2008). In addition, both the global random forest, local RAN₁₅
816 calibrations and the $\delta^{18}\text{O}$ record allowed the identification of several climatic events in the
817 Northern hemisphere, in agreement with the reconstructed total solar irradiance (TSI,
818 Steinhilber et al., 2009, Fig. 10d). Thus, both models highlighted, with slightly different
819 amplitudes, the Medieval Warm Period (800-1000 years BP) and Little Ice Age (LIA; 200-500
820 years BP) periods (Mann et al., 2008; Ljungqvist, 2010; Wang et al., 2018). The LIA event is
821 particularly well represented by the global random forest calibration, in line with the decrease
822 in the TSI (Fig. 10b,d) associated with a relative increase in the $\delta^{18}\text{O}$ of HS4 carbonates
823 (dry/cool event, Wang et al., 2018). Before the MWP, the global random forest calibration
824 shows slight oscillations, which can be assumed to be representative of TSI variations between
825 500 and 1,300 yrs BP. Similarly, an important cooling event, well correlated with a significant
826 decrease in the TSI (Fig. 10a, b, d), was recorded by the two calibrations at 1300 yrs BP.

827 The global random forest calibration also highlighted two cooling events, poorly
828 represented by the local RAN₁₅ calibration: one at ca. 4,200 yrs BP ago and, to a lesser extent,
829 another one between 2,800 and 3,000 yrs BP (Bond et al., 2001; Mayewski et al., 2004). The
830 event at 4,200 yrs BP is consistent with the $\delta^{18}\text{O}$ and solar irradiance records and is referenced
831 in the literature as the "4.2 kiloyear event" (deMenocal, 2001). This intense drought event was
832 suggested to have had a major impact on different civilizations (collapses, migrations;
833 (Gibbons, 1993; Staubwasser et al., 2003; Li et al., 2018; Bini et al., 2019). Thus, in some parts
834 of China, the production of rice fields sharply decreased during this period, leading to a decrease
835 in population (Gao et al., 2007).

836 Both calibrations additionally shows a cooling period between 4,000 yrs and 3,200 yrs
837 BP, more pronounced based on the global random forest model, followed by another cooling
838 between 3,200 years BP and 3,000 yrs BP. This cooling period is consistent with the trends
839 derived from $\delta^{18}\text{O}$ and solar irradiance records. It culminates with a cold episode at 3000 yrs
840 BP, also known as Late Bronze Age Collapse (Kaniewski et al., 2013). Indeed, this cold
841 episode, combined with droughts, may have led to a decrease in agricultural production in
842 China, contributing to the degradation of trade routes and ultimately to the collapse of Bronze
843 Age civilizations (Weiss, 1982; Knapp and Manning, 2016). Last, the global random forest
844 calibration also highlights two additional cold events, between 5,600 and 5,900 yrs BP, as well
845 as around 7,100 yrs BP, corresponding to solar irradiance minima (Bond et al., 2001; Mayewski
846 et al., 2004) and which are not as clearly visible with the local RAN₁₅ calibration by Wang et
847 al. (2016).

848 The first application of the random forest calibration to a natural archive shows the
849 potential of 3-OH FAs as paleotemperature proxies at a global scale, as known and documented
850 climatic events were recorded, with a similar RMSE (2.8 °C; Table 2) as that of the local
851 calibration by Wang et al. (2.6 °C; 2016). In summary, we demonstrate that 3-OH FAs are
852 promising and effective temperature proxies for terrestrial settings, complementary to, and
853 independent of, the brGDGTs (De Jonge et al., 2014; Naafs et al., 2017; Dearing Crampton-
854 Flood et al., 2020), and also highlight the usefulness of non-parametric models using machine
855 learning, especially the random forest algorithm, to establish global MAAT calibrations. We
856 expect that analyses of 3-OH FAs in a larger number of globally distributed soils will further
857 improve the accuracy and robustness of the global random forest calibration for
858 paleotemperature reconstruction. Additional paleoapplications are also required to further test
859 and validate the applicability of the global MAAT and pH calibrations based on 3-OH FAs
860 presented in this study.

861

862 **5. Conclusions**

863 3-OH FAs have been recently proposed as environmental proxies in terrestrial settings,
864 based on local studies. This study investigated for the first time the applicability of these
865 compounds as MAAT and pH proxies at the global scale using an extended soil dataset across
866 a series of globally distributed elevation transects ($n = 168$). Strong linear relationships between
867 3-OH FA-derived indices (RAN₁₅, RAN₁₇ and RIAN) and MAAT/pH could only be obtained
868 locally, for some individual transects, suggesting that these indices cannot be used as
869 paleoproxies at the global scale through this kind of model. Other algorithms (multiple linear
870 regression, k-NN and random forest models) were tested and, in contrast with simple linear
871 regressions, provided strong global correlations between MAAT/pH and 3-OH FA relative
872 abundances. The applicability of these three models for paleotemperature reconstruction was
873 tested and compared with the MAAT record from the unique available record: a Chinese
874 speleothem. The calibration based on the random forest model appeared to be the most robust
875 and showed similar trends to previous reconstructions and known Holocene climate variations.
876 Furthermore, the global random forest model highlighted documented climatic events poorly
877 represented by the local RAN₁₅ calibration. This new global model is promising for
878 paleotemperature reconstructions in terrestrial settings and could be further improved by
879 analyzing 3-OH FAs in a larger number of globally distributed soils. This study demonstrates

880 the major potential of 3-OH FAs as MAAT/pH proxies in terrestrial environments through the
881 different models presented and their application for paleoreconstruction.

882

883 **Data availability.** All data are available in the Supplementary tables.

884

885 **Author contributions.** P.V. performed the lipid and statistical analyses and wrote a first draft
886 of the paper., A.H. and S.D. supervised the work of P.V. and corrected the first draft, P.V. and
887 A.T. developed the different models, G.B., A.N., W.P.S., N.S., J.P.W. and S.C. provided
888 samples and/or associated data, and all the co-authors reviewed and commented on the paper.

889

890 **Competing interests.** The authors declare that they have no conflict of interest.

891

892 **Acknowledgments.** We thank Sorbonne Université for a PhD scholarship to P.V. and the Labex
893 MATISSE (Sorbonne Université) for financial support. The EC2CO program (CNRS/INSU –
894 BIOHEFECT/MICROBIEN) is thanked for funding of the SHAPE project. A.H. and S.C. are
895 grateful for funding of the ECOS SUD/ ECOS ANID #C19U01 project. We are grateful to
896 Jérôme Poulenard for discussions on soil characteristics, and for comments on the manuscript.
897 We thank Dr. Juntao Wang and Prof. Jinzheng He for having provided soils from Mt. Shegyla.
898 We thank the Peruvian program led by NS, including CONCYTEC/FONDECYT through
899 contract 116-2016. We thank the associate editor Dr. van der Meer and the reviewers for their
900 comments which helped in improving the manuscript.

901 **References**

902 Beales, N.: Adaptation of Microorganisms to Cold Temperatures, Weak Acid Preservatives,
903 Low pH, and Osmotic Stress: A Review, 3, 1–20, <https://doi.org/10.1111/j.1541-4337.2004.tb00057.x>, 2004.

905 Bhat, U. R. and Carlson, R. W.: A new method for the analysis of amide-linked hydroxy fatty
906 acids in lipid-As from gram-negative bacteria, Glycobiology, 2, 535–539,
907 <https://doi.org/10.1093/glycob/2.6.535>, 1992.

908 Bini, M., Zanchetta, G., Persouli, A., Cartier, R., Catala, A., Cacho, I., Dean, J. R., Di Rita, F.,
909 Drysdale, R. N., Finné, M., Isola, I., Jalali, B., Lirer, F., Magri, D., Masi, A., Marks, L., Mercuri,
910 A. M., Peyron, O., Sadori, L., Sicre, M.-A., Welc, F., Zielhofer, C., and Brisset, E.: The 4.2 ka
911 BP Event in the Mediterranean region : an overview, 15, 555–577, 2019.

912 Bonanomi, G., Zotti, M., Mogavero, V., Cesarano, G., Saulino, L., Rita, A., Tesei, G.,
913 Allegrezza, M., Saracino, A., and Allevato, E.: Climatic and anthropogenic factors explain the
914 variability of *Fagus sylvatica* treeline elevation in fifteen mountain groups across the
915 Apennines, Forest Ecosystems, 7, 5, <https://doi.org/10.1186/s40663-020-0217-8>, 2020.

916 Bond, G., Kromer, B., Beer, J., Muscheler, R., Evans, M. N., Showers, W., Hoffmann, S., Lotti-
917 Bond, R., Hajdas, I., and Bonani, G.: Persistent Solar Influence on North Atlantic Climate
918 During the Holocene, 294, 2130–2136, <https://doi.org/10.1126/science.1065680>, 2001.

919 Brassell, S. C., Eglington, G., Marlowe, I. T., Pflaumann, U., and Sarnthein, M.: Molecular
920 stratigraphy: a new tool for climatic assessment, 320, 129–133,
921 <https://doi.org/10.1038/320129a0>, 1986.

922 Breiman, L.: Random Forests, Machine Learning, 45, 5–32,
923 <https://doi.org/10.1023/A:1010933404324>, 2001.

924 Carter, M. R., Gregorich, E. G., and Gregorich, E. G.: Soil Sampling and Methods of Analysis,
925 CRC Press, <https://doi.org/10.1201/9781420005271>, 2007.

926 Coffinet, S., Huguet, A., Williamson, D., Fosse, C., and Derenne, S.: Potential of GDGTs as a
927 temperature proxy along an altitudinal transect at Mount Rungwe (Tanzania), Organic
928 Geochemistry, 68, 82–89, <https://doi.org/10.1016/j.orggeochem.2014.01.004>, 2014.

929 Coffinet, S., Huguet, A., Pedentchouk, N., Bergonzini, L., Omuombo, C., Williamson, D.,
930 Anquetil, C., Jones, M., Majule, A., Wagner, T., and Derenne, S.: Evaluation of branched
931 GDGTs and leaf wax n-alkane δ 2H as (paleo) environmental proxies in East Africa,
932 Geochimica et Cosmochimica Acta, 198, 182–193, <https://doi.org/10.1016/j.gca.2016.11.020>,
933 2017.

934 Coffinet, S., Huguet, A., Bergonzini, L., Pedentchouk, N., Williamson, D., Anquetil, C., Gałka,
935 M., Kołaczek, P., Karpińska-Kołaczek, M., Majule, A., Laggoun-Défarge, F., Wagner, T., and
936 Derenne, S.: Impact of climate change on the ecology of the Kyambangunguru crater marsh in
937 southwestern Tanzania during the Late Holocene, Quaternary Science Reviews, 196, 100–117,
938 <https://doi.org/10.1016/j.quascirev.2018.07.038>, 2018.

939 De Jonge, C., Hopmans, E. C., Zell, C. I., Kim, J.-H., Schouten, S., and Sinninghe Damsté, J.
940 S.: Occurrence and abundance of 6-methyl branched glycerol dialkyl glycerol tetraethers in

941 soils: Implications for palaeoclimate reconstruction, *Geochimica et Cosmochimica Acta*, 141,
942 97–112, <https://doi.org/10.1016/j.gca.2014.06.013>, 2014.

943 De Jonge, C., Radujković, D., Sigurdsson, B. D., Weedon, J. T., Janssens, I., and Peterse, F.:
944 Lipid biomarker temperature proxy responds to abrupt shift in the bacterial community
945 composition in geothermally heated soils, *Organic Geochemistry*, 137, 103897,
946 <https://doi.org/10.1016/j.orggeochem.2019.07.006>, 2019.

947 Dearing Crampton-Flood, E., Tierney, J. E., Peterse, F., Kirkels, F. M. S. A., and Sinninghe
948 Damsté, J. S.: BayMBT: A Bayesian calibration model for branched glycerol dialkyl glycerol
949 tetraethers in soils and peats, *Geochimica et Cosmochimica Acta*, 268, 142–159,
950 <https://doi.org/10.1016/j.gca.2019.09.043>, 2020.

951 deMenocal, P. B.: Cultural Responses to Climate Change During the Late Holocene, 292, 667–
952 673, <https://doi.org/10.1126/science.1059287>, 2001.

953 Denich, T. J., Beaudette, L. A., Lee, H., and Trevors, J. T.: Effect of selected environmental
954 and physico-chemical factors on bacterial cytoplasmic membranes, *Journal of Microbiological
955 Methods*, 52, 149–182, [https://doi.org/10.1016/S0167-7012\(02\)00155-0](https://doi.org/10.1016/S0167-7012(02)00155-0), 2003.

956 Denisko, D. and Hoffman, M. M.: Classification and interaction in random forests, *Proc Natl
957 Acad Sci USA*, 115, 1690–1692, <https://doi.org/10.1073/pnas.1800256115>, 2018.

958 Dunkley Jones, T., Eley, Y.L., Thomson, W., Greene, S.E., Mandel, I., Edgar, K., Bendle, J.A.,
959 OPTiMAL: a new machine learning approach for GDGT-based palaeothermometry. *Climate of
960 the Past* 16, 2599–2617, 2020.

961 Eglinton, T. I. and Eglinton, G.: Molecular proxies for paleoclimatology, *Earth and Planetary
962 Science Letters*, 275, 1–16, <https://doi.org/10.1016/j.epsl.2008.07.012>, 2008.

963 Emiliani, C.: Pleistocene Temperatures, *The Journal of Geology*, 63, 538–578,
964 <https://doi.org/10.1086/626295>, 1955.

965 Erez, J. and Luz, B.: Experimental paleotemperature equation for planktonic foraminifera,
966 *Geochimica et Cosmochimica Acta*, 47, 1025–1031, [https://doi.org/10.1016/0016-7037\(83\)90232-6](https://doi.org/10.1016/0016-7037(83)90232-6), 1983.

968 Gangopadhyay, S., Harding, B. L., Rajagopalan, B., Lukas, J. J., and Fulp, T. J.: A
969 nonparametric approach for paleohydrologic reconstruction of annual streamflow ensembles,
970 45, <https://doi.org/10.1029/2008WR007201>, 2009.

971 Gao, H., Zhu, C., and Xu, W.: Environmental change and cultural response around 4200 cal. yr
972 BP in the Yishu River Basin, Shandong, *J GEOGR SCI*, 17, 285–292,
973 <https://doi.org/10.1007/s11442-007-0285-5>, 2007.

974 Gibbons, A.: How the Akkadian Empire Was Hung Out to Dry, *Science*, 261, 985,
975 <https://doi.org/10.1126/science.261.5124.985>, 1993.

976 Hazel, J. R. and Eugene Williams, E.: The role of alterations in membrane lipid composition in
977 enabling physiological adaptation of organisms to their physical environment, *Progress in Lipid
978 Research*, 29, 167–227, [https://doi.org/10.1016/0163-7827\(90\)90002-3](https://doi.org/10.1016/0163-7827(90)90002-3), 1990.

979 Hofmann, K., Lamprecht, A., Pauli, H., and Illmer, P.: Distribution of Prokaryotic Abundance
980 and Microbial Nutrient Cycling Across a High-Alpine Altitudinal Gradient in the Austrian
981 Central Alps is Affected by Vegetation, Temperature, and Soil Nutrients, *Microb Ecol*, 72, 704–
982 716, <https://doi.org/10.1007/s00248-016-0803-z>, 2016.

983 Hu, C., Henderson, G. M., Huang, J., Xie, S., Sun, Y., and Johnson, K. R.: Quantification of
984 Holocene Asian monsoon rainfall from spatially separated cave records, *Earth and Planetary
985 Science Letters*, 266, 221–232, <https://doi.org/10.1016/j.epsl.2007.10.015>, 2008.

986 Huguet, A., Coffinet, S., Roussel, A., Gayraud, F., Anquetil, C., Bergonzini, L., Bonanomi, G.,
987 Williamson, D., Majule, A., and Derenne, S.: Evaluation of 3-hydroxy fatty acids as a pH and
988 temperature proxy in soils from temperate and tropical altitudinal gradients, *Organic
989 Geochemistry*, 129, 1–13, <https://doi.org/10.1016/j.orggeochem.2019.01.002>, 2019.

990 Huguet, C., Hopmans, E. C., Febo-Ayala, W., Thompson, D. H., Sinninghe Damsté, J. S., and
991 Schouten, S.: An improved method to determine the absolute abundance of glycerol
992 dibiphytanyl glycerol tetraether lipids, *Organic Geochemistry*, 37, 1036–1041,
993 <https://doi.org/10.1016/j.orggeochem.2006.05.008>, 2006.

994 Kaniewski, D., Campo, E. V., Guiot, J., Burel, S. L., Otto, T., and Baeteman, C.: Environmental
995 Roots of the Late Bronze Age Crisis, *PLOS ONE*, 8, e71004,
996 <https://doi.org/10.1371/journal.pone.0071004>, 2013.

997 Knapp, A. B. and Manning, S. W.: Crisis in Context: The End of the Late Bronze Age in the
998 Eastern Mediterranean, 120, 99–149, <https://doi.org/10.3764/aja.120.1.0099>, 2016.

999 Li, C.-H., Li, Y.-X., Zheng, Y.-F., Yu, S.-Y., Tang, L.-Y., Li, B.-B., and Cui, Q.-Y.: A high-
1000 resolution pollen record from East China reveals large climate variability near the
1001 Northgrippian-Meghalayan boundary (around 4200 years ago) exerted societal influence,
1002 *Palaeogeography, Palaeoclimatology, Palaeoecology*, 512, 156–165,
1003 <https://doi.org/10.1016/j.palaeo.2018.07.031>, 2018.

1004 Liu, Z., Zhu, J., Rosenthal, Y., Zhang, X., Otto-Bliesner, B. L., Timmermann, A., Smith, R. S.,
1005 Lohmann, G., Zheng, W., and Elison Timm, O.: The Holocene temperature conundrum, *Proc
1006 Natl Acad Sci U S A*, 111, E3501–E3505, <https://doi.org/10.1073/pnas.1407229111>, 2014.

1007 Ljungqvist, F. C.: A new reconstruction of temperature variability in the extra-tropical northern
1008 hemisphere during the last two millennia, 92, 339–351, [https://doi.org/10.1111/j.1468-0459.2010.00399.x](https://doi.org/10.1111/j.1468-
1009 0459.2010.00399.x), 2010.

1010 Loomis, S. E., Russell, J. M., Ladd, B., Street-Perrott, F. A., and Sinninghe Damsté, J. S.: Calibration and application of the branched GDGT temperature proxy on East African lake
1011 sediments, *Earth and Planetary Science Letters*, 357–358, 277–288,
1012 <https://doi.org/10.1016/j.epsl.2012.09.031>, 2012.

1013 Malhi, Y., Silman, M., Salinas, N., Bush, M., Meir, P., and Saatchi, S.: Introduction: Elevation
1014 gradients in the tropics: laboratories for ecosystem ecology and global change research, 16,
1015 3171–3175, <https://doi.org/10.1111/j.1365-2486.2010.02323.x>, 2010.

1016 Mann, M. E., Zhang, Z., Hughes, M. K., Bradley, R. S., Miller, S. K., Rutherford, S., and Ni,
1017 F.: Proxy-based reconstructions of hemispheric and global surface temperature variations over
1018

1019 the past two millennia, *Proceedings of the National Academy of Sciences*, 105, 13252–13257,
1020 <https://doi.org/10.1073/pnas.0805721105>, 2008.

1021 Margesin, R., Jud, M., Tscherko, D., and Schinner, F.: Microbial communities and activities in
1022 alpine and subalpine soils: Communities and activities in alpine and subalpine soils, 67, 208–
1023 218, <https://doi.org/10.1111/j.1574-6941.2008.00620.x>, 2009.

1024 Mayewski, P. A., Rohling, E. E., Curt Stager, J., Karlén, W., Maasch, K. A., David Meeker, L.,
1025 Meyerson, E. A., Gasse, F., van Kreveld, S., Holmgren, K., Lee-Thorp, J., Rosqvist, G., Rack,
1026 F., Staubwasser, M., Schneider, R. R., and Steig, E. J.: Holocene climate variability, *Quaternary*
1027 *Research*, 62, 243–255, <https://doi.org/10.1016/j.yqres.2004.07.001>, 2004.

1028 Naafs, B. D. A., Gallego-Sala, A. V., Inglis, G. N., and Pancost, R. D.: Refining the global
1029 branched glycerol dialkyl glycerol tetraether (brGDGT) soil temperature calibration, *Organic*
1030 *Geochemistry*, 106, 48–56, <https://doi.org/10.1016/j.orggeochem.2017.01.009>, 2017.

1031 Nottingham, A. T., Whitaker, J., Turner, B. L., Salinas, N., Zimmermann, M., Malhi, Y., and
1032 Meir, P.: Climate Warming and Soil Carbon in Tropical Forests: Insights from an Elevation
1033 Gradient in the Peruvian Andes, 65, 906–921, <https://doi.org/10.1093/biosci/biv109>, 2015.

1034 Nottingham, A. T., Fierer, N., Turner, B. L., Whitaker, J., Ostle, N. J., McNamara, N. P.,
1035 Bardgett, R. D., Leff, J. W., Salinas, N., Silman, M. R., Kruuk, L. E. B., and Meir, P.: Microbes
1036 follow Humboldt: temperature drives plant and soil microbial diversity patterns from the
1037 Amazon to the Andes, 99, 2455–2466, <https://doi.org/10.1002/ecy.2482>, 2018.

1038 Peterse, F., Kim, J.-H., Schouten, S., Kristensen, D. K., Koç, N., and Sinninghe Damsté, J. S.:
1039 Constraints on the application of the MBT/CBT palaeothermometer at high latitude
1040 environments (Svalbard, Norway), *Organic Geochemistry*, 40, 692–699,
1041 <https://doi.org/10.1016/j.orggeochem.2009.03.004>, 2009.

1042 Peterse, F., van der Meer, J., Schouten, S., Weijers, J. W. H., Fierer, N., Jackson, R. B., Kim,
1043 J.-H., and Sinninghe Damsté, J. S.: Revised calibration of the MBT–CBT paleotemperature
1044 proxy based on branched tetraether membrane lipids in surface soils, *Geochimica et*
1045 *Cosmochimica Acta*, 96, 215–229, <https://doi.org/10.1016/j.gca.2012.08.011>, 2012.

1046 Peterse, F., Moy, C. M., and Eglinton, T. I.: A laboratory experiment on the behaviour of soil-
1047 derived core and intact polar GDGTs in aquatic environments, *Biogeosciences*, 12, 933–943,
1048 <https://doi.org/10.5194/bg-12-933-2015>, 2015.

1049 R Core Team, R: A language and environment for statistical computing. R Foundation for
1050 Statistical Computing, Vienna, Austria, 2014.

1051 Russell, N. J., Evans, R. I., ter Steeg, P. F., Hellemons, J., Verheul, A., and Abee, T.:
1052 Membranes as a target for stress adaptation, *International Journal of Food Microbiology*, 28,
1053 255–261, [https://doi.org/10.1016/0168-1605\(95\)00061-5](https://doi.org/10.1016/0168-1605(95)00061-5), 1995.

1054 Russell, J. M., Hopmans, E. C., Loomis, S. E., Liang, J., and Sinninghe Damsté, J. S.:
1055 Distributions of 5- and 6-methyl branched glycerol dialkyl glycerol tetraethers (brGDGTs) in
1056 East African lake sediment: Effects of temperature, pH, and new lacustrine paleotemperature
1057 calibrations, *Organic Geochemistry*, 117, 56–69,
1058 <https://doi.org/10.1016/j.orggeochem.2017.12.003>, 2018.

1059 Scalercio, S., Bonacci, T., Mazzei, A., Pizzolotto, R., and Brandmayr, P.: Better up, worse
1060 down: bidirectional consequences of three decades of climate change on a relict population of
1061 *Erebia cassioides*, *J Insect Conserv*, 18, 643–650, <https://doi.org/10.1007/s10841-014-9669-x>,
1062 2014.

1063 Schouten, S., Hopmans, E. C., and Sinninghe Damsté, J. S.: The organic geochemistry of
1064 glycerol dialkyl glycerol tetraether lipids: A review, *Organic Geochemistry*, 54, 19–61,
1065 <https://doi.org/10.1016/j.orggeochem.2012.09.006>, 2013.

1066 Siles, J. A. and Margesin, R.: Abundance and Diversity of Bacterial, Archaeal, and Fungal
1067 Communities Along an Altitudinal Gradient in Alpine Forest Soils: What Are the Driving
1068 Factors?, *Microb Ecol*, 72, 207–220, <https://doi.org/10.1007/s00248-016-0748-2>, 2016.

1069 Sinensky, M.: Homeoviscous Adaptation—A Homeostatic Process that Regulates the Viscosity
1070 of Membrane Lipids in *Escherichia coli*, *PNAS*, 71, 522–525,
1071 <https://doi.org/10.1073/pnas.71.2.522>, 1974.

1072 Singer, S. J. and Nicolson, G. L.: The Fluid Mosaic Model of the Structure of Cell Membranes,
1073 175, 720–731, <https://doi.org/10.1126/science.175.4023.720>, 1972.

1074 Sinninghe Damsté, J. S., Rijpstra, W. I. C., Hopmans, E. C., Weijers, J. W. H., Foesel, B. U.,
1075 Overmann, J. and Dedysh, S. N.: 13,16-Dimethyl Octacosanedioic Acid (iso-Diabolic Acid), a
1076 Common Membrane-Spanning Lipid of Acidobacteria Subdivisions 1 and 3, *Appl. Environ.*
1077 *Microbiol.*, 77(12), 4147–4154, doi:10.1128/AEM.00466-11, 2011.

1078 Sinninghe Damsté, J. S., Rijpstra, W. I. C., Hopmans, E. C., Foesel, B. U., Wüst, P. K.,
1079 Overmann, J., Tank, M., Bryant, D. A., Dunfield, P. F., Houghton, K. and Stott, M. B.: Ether-
1080 and Ester-Bound iso-Diabolic Acid and Other Lipids in Members of Acidobacteria Subdivision
1081 4, *Appl. Environ. Microbiol.*, 80(17), 5207–5218, doi:10.1128/AEM.01066-14, 2014.

1082 Sinninghe Damste, J. S., Rijpstra, W. I. C., Foesel, B. U., Huber, K. J., Overmann, J.,
1083 Nakagawa, S., Kim, J. J., Dunfield, P. F., Dedysh, S. N. and Villanueva, L.: An overview of the
1084 occurrence of ether- and ester-linked iso-diabolic acid membrane lipids in microbial cultures of
1085 the Acidobacteria: Implications for brGDGT paleoproxies for temperature and pH, *Org.*
1086 *Geochem.*, 124, 63–76, doi:10.1016/j.orggeochem.2018.07.006, 2018.

1087 Staubwasser, M., Sirocko, F., Grootes, P. M., and Segl, M.: Climate change at the 4.2 ka BP
1088 termination of the Indus valley civilization and Holocene south Asian monsoon variability,
1089 *Geophysical Research Letters*, 30, 1425, <https://doi.org/10.1029/2002GL016822>, 2003.

1090 Steinhilber, F., Beer, J., and Fröhlich, C.: Total solar irradiance during the Holocene, 36,
1091 <https://doi.org/10.1029/2009GL040142>, 2009.

1092 Szponar, B., Kraśnik, L., Hryniewiecki, T., Gamian, A., and Larsson, L.: Distribution of 3-
1093 Hydroxy Fatty Acids in Tissues after Intraperitoneal Injection of Endotoxin, *Clin Chem*, 49,
1094 1149–1153, <https://doi.org/10.1373/49.7.1149>, 2003.

1095 Tierney, J. E. and Russell, J. M.: Distributions of branched GDGTs in a tropical lake system:
1096 Implications for lacustrine application of the MBT/CBT paleoproxy, *Organic Geochemistry*,
1097 40, 1032–1036, <https://doi.org/10.1016/j.orggeochem.2009.04.014>, 2009.

1098 Tierney, J. E. and Tingley, M. P.: A Bayesian, spatially-varying calibration model for the
1099 TEX86 proxy, *Geochimica et Cosmochimica Acta*, 127, 83–106,
1100 <https://doi.org/10.1016/j.gca.2013.11.026>, 2014.

1101 Todaro, L., Andreu-Hayles, L., D'Alessandro, C., Gutiérrez, E., Cherubini, P., and Saracino,
1102 A.: Response of *Pinus leucodermis* to climate and anthropogenic activity in the National Park
1103 of Pollino (Basilicata, Southern Italy), *Biological Conservation*, 137, 507–519,
1104 <https://doi.org/10.1016/j.biocon.2007.03.010>, 2007.

1105 Véquaud, P., Derenne, S., Anquetil, C., Collin, S., Poulenard, J., Sabatier, P., and Huguet, A.:
1106 Influence of environmental parameters on the distribution of bacterial lipids in soils from the
1107 French Alps: Implications for paleo-reconstructions, *Organic Geochemistry*, 153, 104194,
1108 <https://doi.org/10.1016/j.orggeochem.2021.104194>, 2021.

1109 Wakeham, S. G., Pease, T. K., and Benner, R.: Hydroxy fatty acids in marine dissolved organic
1110 matter as indicators of bacterial membrane material, *Organic Geochemistry*, 34, 857–868,
1111 [https://doi.org/10.1016/S0146-6380\(02\)00189-4](https://doi.org/10.1016/S0146-6380(02)00189-4), 2003.

1112 Wang, C., Bendle, J., Yang, Y., Yang, H., Sun, H., Huang, J., and Xie, S.: Impacts of pH and
1113 temperature on soil bacterial 3-hydroxy fatty acids: Development of novel terrestrial proxies,
1114 *Organic Geochemistry*, 94, 21–31, <https://doi.org/10.1016/j.orggeochem.2016.01.010>, 2016.

1115 Wang, C., Bendle, J. A., Zhang, H., Yang, Y., Liu, D., Huang, J., Cui, J., and Xie, S.: Holocene
1116 temperature and hydrological changes reconstructed by bacterial 3-hydroxy fatty acids in a
1117 stalagmite from central China, *Quaternary Science Reviews*, 192, 97–105,
1118 <https://doi.org/10.1016/j.quascirev.2018.05.030>, 2018.

1119 Wang, H., An, Z., Lu, H., Zhao, Z., and Liu, W.: Calibrating bacterial tetraether distributions
1120 towards in situ soil temperature and application to a loess-paleosol sequence, *Quaternary
1121 Science Reviews*, 231, 106172, <https://doi.org/10.1016/j.quascirev.2020.106172>, 2020.

1122 Wang, J.-T., Cao, P., Hu, H.-W., Li, J., Han, L.-L., Zhang, L.-M., Zheng, Y.-M., and He, J.-Z.:
1123 Altitudinal Distribution Patterns of Soil Bacterial and Archaeal Communities Along Mt.
1124 Shegyla on the Tibetan Plateau, *Microb Ecol*, 69, 135–145, <https://doi.org/10.1007/s00248-014-0465-7>, 2015.

1126 Weber, Y., De Jonge, C., Rijpstra, W. I. C., Hopmans, E. C., Stadnitskaia, A., Schubert, C. J.,
1127 Lehmann, M. F., Sinninghe Damsté, J. S., and Niemann, H.: Identification and carbon isotope
1128 composition of a novel branched GDGT isomer in lake sediments: Evidence for lacustrine
1129 branched GDGT production, *Geochimica et Cosmochimica Acta*, 154, 118–129,
1130 <https://doi.org/10.1016/j.gca.2015.01.032>, 2015.

1131 Weijers, J. W. H., Schouten, S., van den Donker, J. C., Hopmans, E. C., and Sinninghe Damsté,
1132 J. S.: Environmental controls on bacterial tetraether membrane lipid distribution in soils,
1133 *Geochimica et Cosmochimica Acta*, 71, 703–713, <https://doi.org/10.1016/j.gca.2006.10.003>,
1134 2007.

1135 Weiss, B.: The decline of Late Bronze Age civilization as a possible response to climatic
1136 change, *Climatic Change*, 4, 173–198, <https://doi.org/10.1007/BF00140587>, 1982.

1137 Whitaker, J., Ostle, N., Nottingham, A. T., Ccahuana, A., Salinas, N., Bardgett, R. D., Meir, P.,
1138 and McNamara, N. P.: Microbial community composition explains soil respiration responses to

1139 changing carbon inputs along an Andes-to-Amazon elevation gradient, 102, 1058–1071,
1140 <https://doi.org/10.1111/1365-2745.12247>, 2014.

1141 Wilkinson, S.G., 1988. Gram-negative bacteria. 935 In: Ratledge C., Wilkinson S.G. (Eds),
1142 Microbial Lipids, vol. 1. Academic Press, New York, pp. 199-488.

1143 Wollenweber, H. W. and Rietschel, E. T.: Analysis of lipopolysaccharide (lipid A) fatty acids.,
1144 11, 195–211, 1990.

1145 Wollenweber, H.-W., Broady, K. W., Luderitz, O., and Rietschel, E. T.: The Chemical Structure
1146 of Lipid A, 124, 191–198, <https://doi.org/10.1111/j.1432-1033.1982.tb05924.x>, 1982.

1147 Yang, H., Lü, X., Ding, W., Lei, Y., Dang, X., and Xie, S.: The 6-methyl branched tetraethers
1148 significantly affect the performance of the methylation index (MBT') in soils from an altitudinal
1149 transect at Mount Shennongjia, Organic Geochemistry, 82, 42–53,
1150 <https://doi.org/10.1016/j.orggeochem.2015.02.003>, 2015.

1151 Zelles, L.: Fatty acid patterns of phospholipids and lipopolysaccharides in the characterisation
1152 of microbial communities in soil: a review, Biol Fertil Soils, 29, 111–129,
1153 <https://doi.org/10.1007/s003740050533>, 1999.

1154

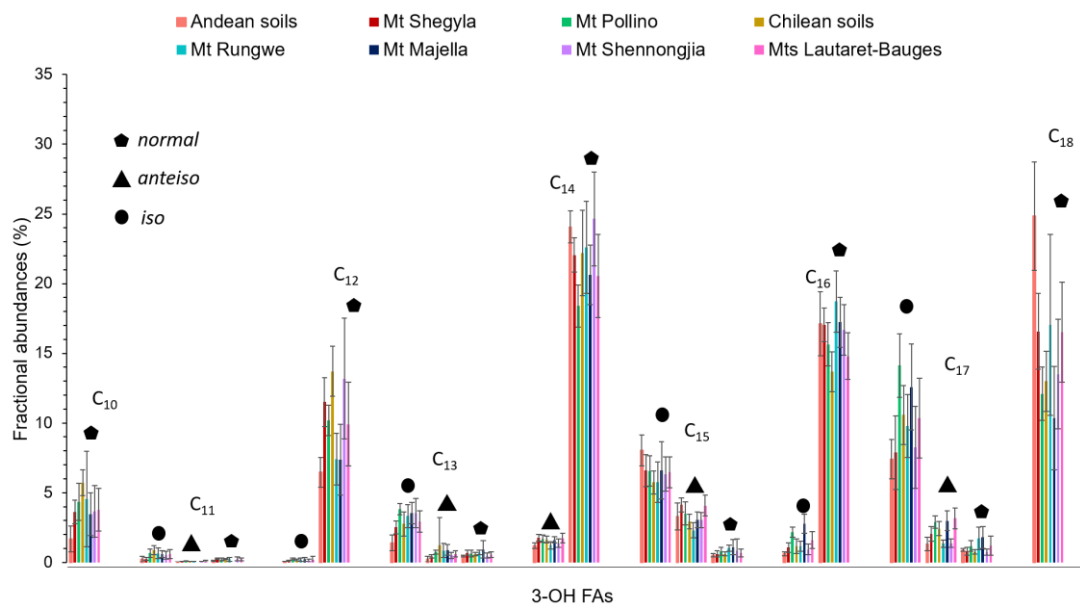


Figure 1. Average distribution of 3-OH FAs along the 8 altitudinal transects investigated in this study. Data from Mts. Majella and Rungwe were taken from Huguet et al. (2019). Data from Mt. Shennongjia were taken from Wang et al. (2016). Data from Mts. Lautaret-Galibier were taken from Véquaud et al. (2021).

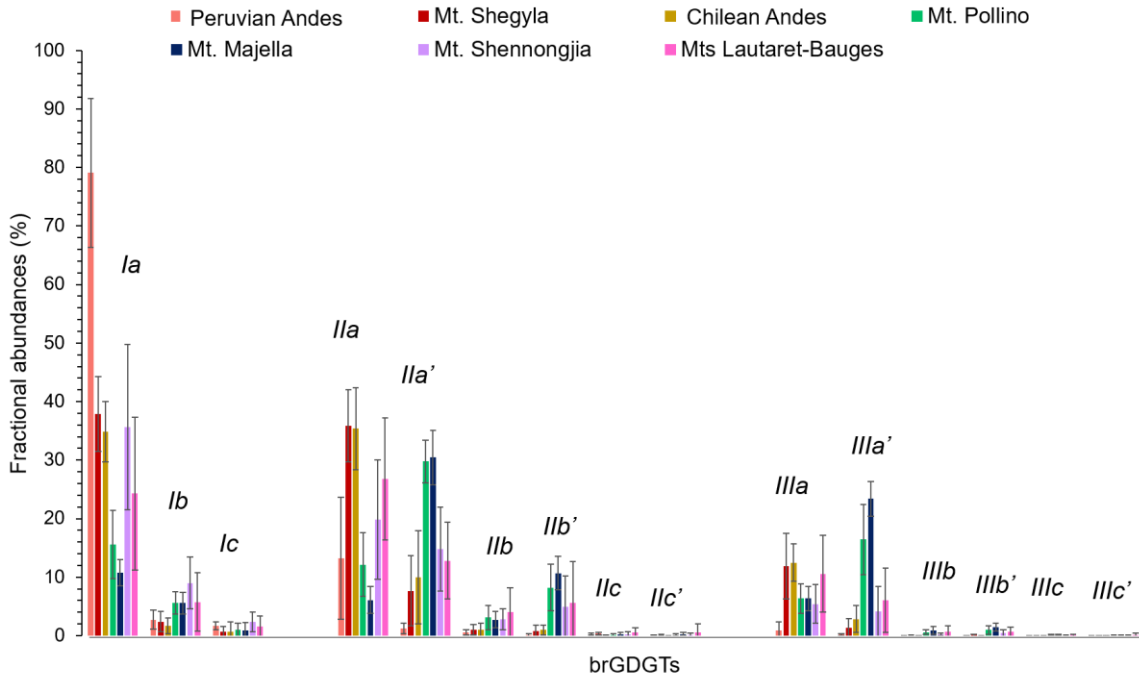


Figure 2. Average distribution of 5- and 6-methyl brGDGTs, along Mts. Shegyla, Pollino Majella, Lautaret-Bauges, Peruvian Andes and Chilean Andes. Data from Mt. Majella were taken from Huguet et al. (2019). Data from Mt. Shennongjia were taken from Yang et al. (2015). Data from Mts. Lautaret-Galibier were taken from Véquaud et al. (2021).

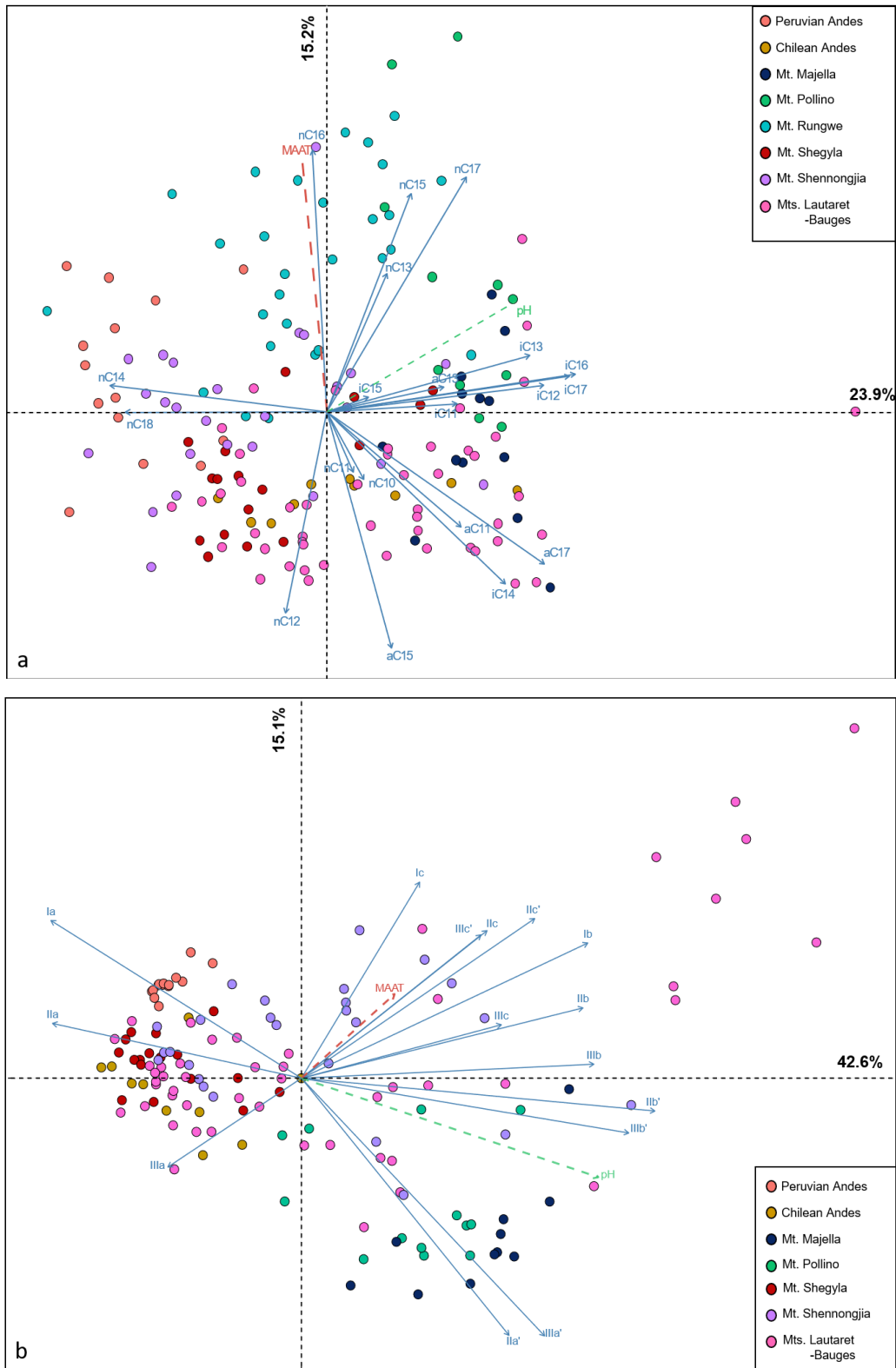


Figure 3. PCA biplot of (a) 3-OH FA fractional abundances in soil samples from the 8 altitudinal transects and (b) brGDGT fractional abundances in soil samples from 7 of the 8 altitudinal transects. BrGDGT data from Mt. Rungwe, for which 5- and 6-methyl isomers were not separated, were not included in the PCA.

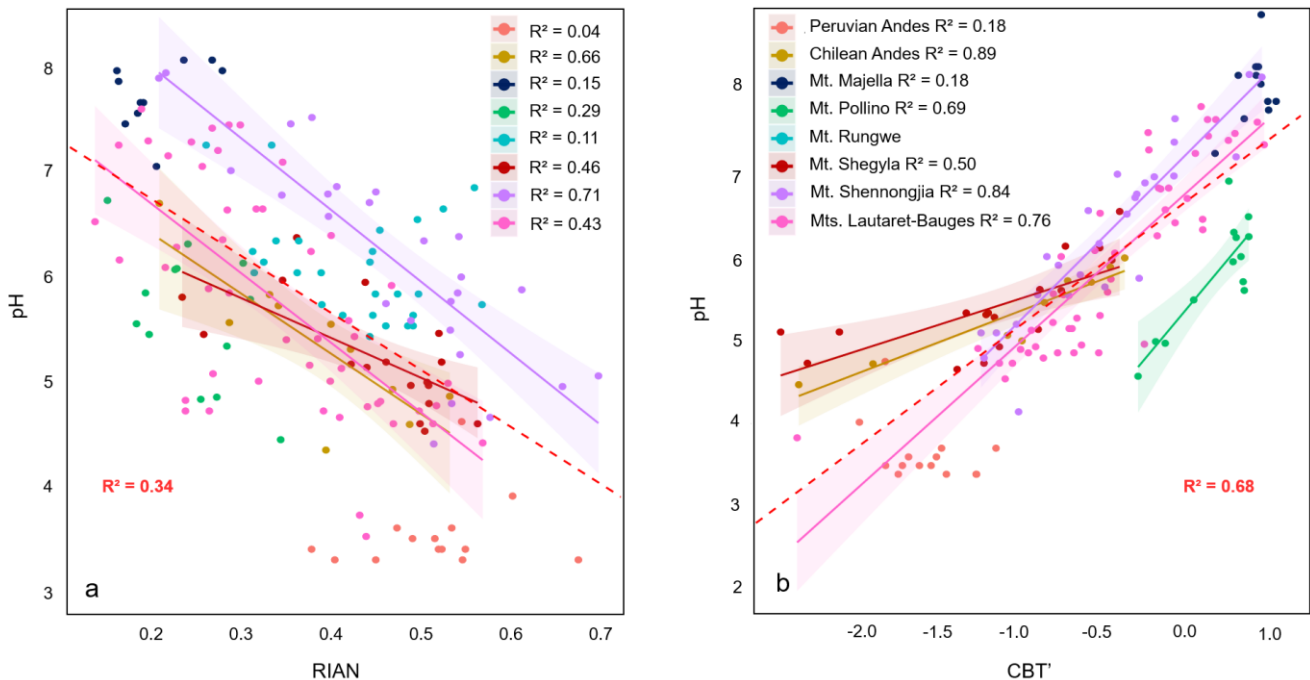


Figure 4. Linear regressions between (a) pH and RIAN and (b) pH and CBT' along the 8 altitudinal transects investigated. Dotted lines represent the 95% confidence interval for each regression and colored areas represent the 95% confidence interval for each regression. Data for Mts. Majella and Rungwe were taken from Huguet et al. (2019). Data from Mt. Shennongjia were taken from Yang et al. (2015) and Wang et al. (2016). Data from Mts. Lautaret-Galibier were taken from Véquaud et al. (2021). Only significant regressions ($p < 0.05$) are shown.

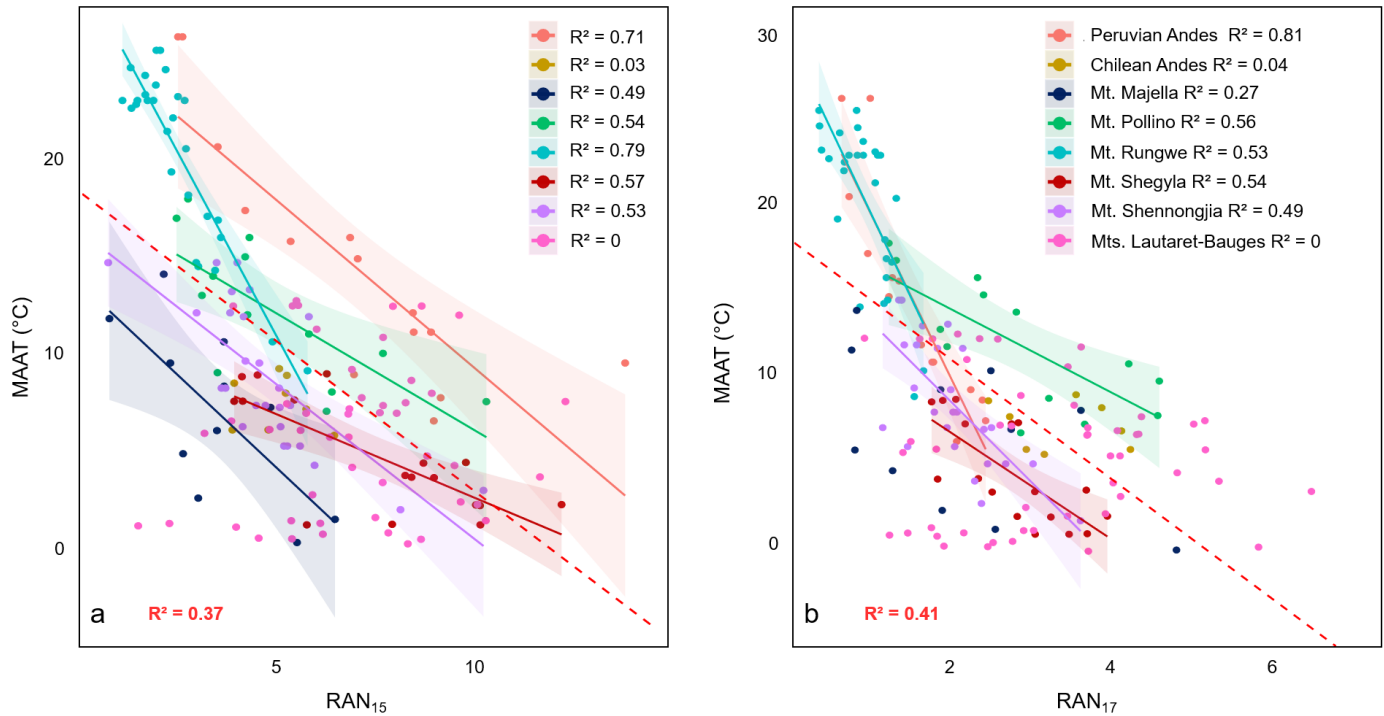


Figure 5. Linear regressions between (a) MAAT and RAN_{15} and (b) MAAT and RAN_{17} along the 8 altitudinal transects investigated. Dotted lines represent the 95% confidence interval for each regression and colored areas represent the 95% confidence interval for each regression. Data from Mts. Majella and Rungwe were taken from Huguet et al. (2019). Data from Mt. Shennongjia were taken from Wang et al. (2016). Data from Mts. Lautaret-Galibier were taken from Véquaud et al. (2021). Only significant regressions ($\text{p} < 0.05$) are shown.

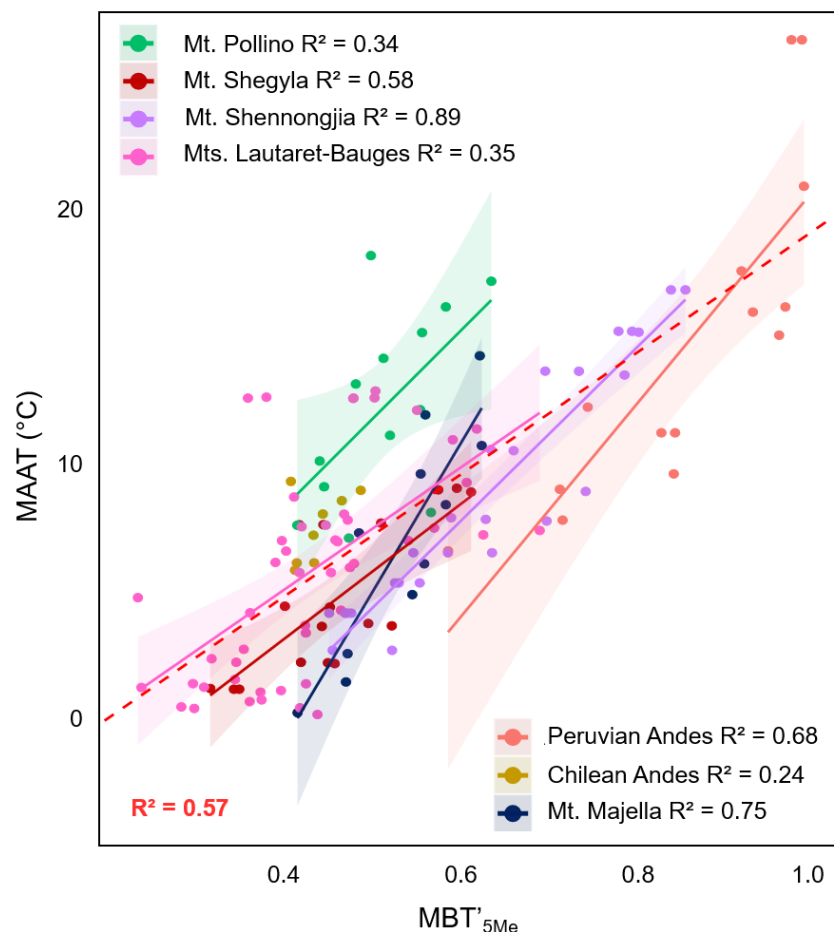


Figure 6. Linear regressions between (a) MAAT and MBT'5Me along 7 of the 8 altitudinal transects investigated. Data from Mt. Rungwe (Coffinet et al., 2014), for which 5- and 6-methyl brGDGTs were not separated, were not included in this graph. Dotted lines represent the 95% confidence interval for each regression and colored areas represent the 95% confidence interval for each regression. Data from Mt. Majella were taken from Huguet et al. (2019). Data from Mts. Lautaret-Galibier were taken from Véquaud et al. (2021). Data from Mt. Shennongjia were taken from Yang et al. (2015). The global soil calibration by De Jonge et al. (2014) was applied to all these transects. Only significant regressions ($p < 0.05$) are shown.

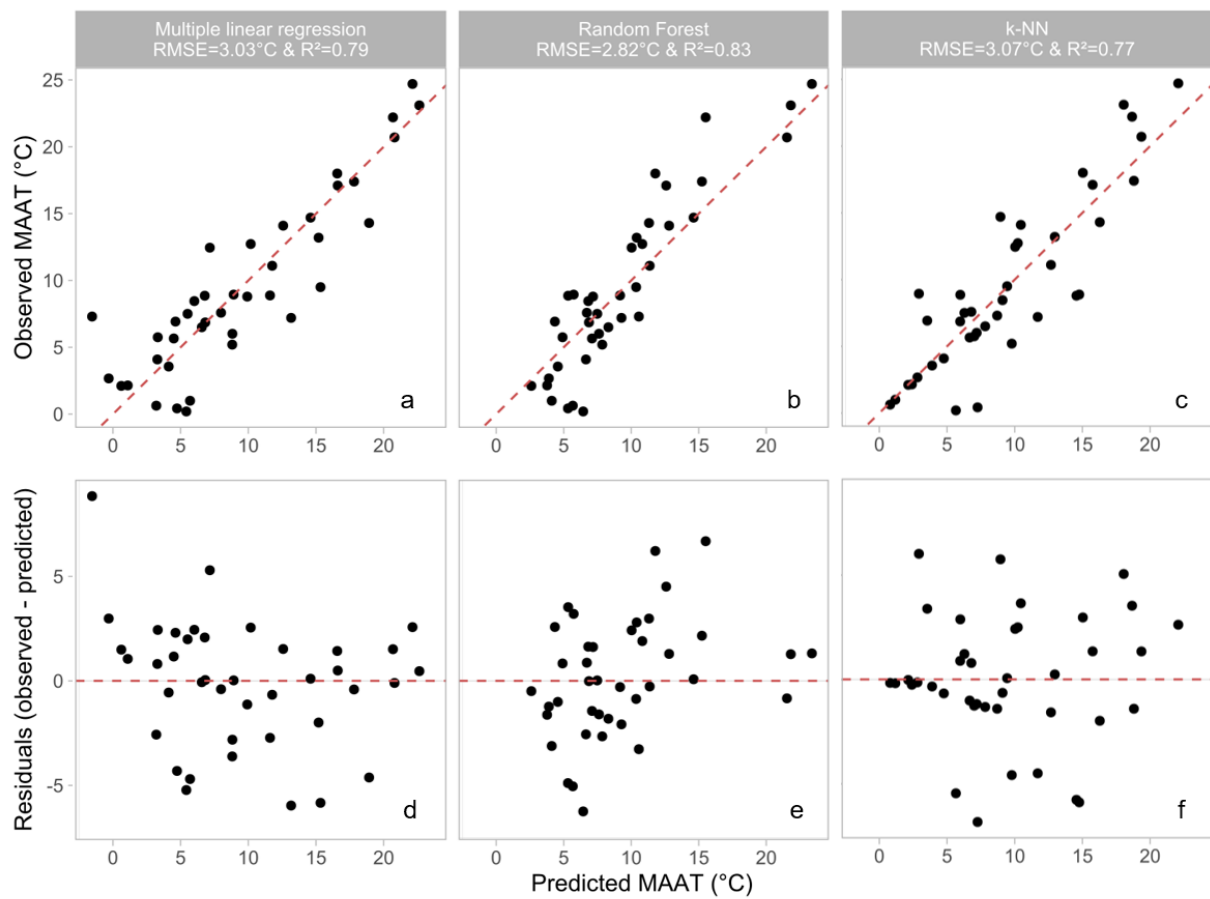


Figure 7. Results of the three different models tested to reconstruct the MAAT from 3-OH FA distribution: observed MAAT (°C) vs Predicted MAAT (°C) for (a) the multiple linear regression model, (b) the random forest model and (c) the k-NN method. MAAT residuals plotted against the predicted MAAT for (d) the multiple linear regression model, (e) the random forest model and (f) the k-NN method.

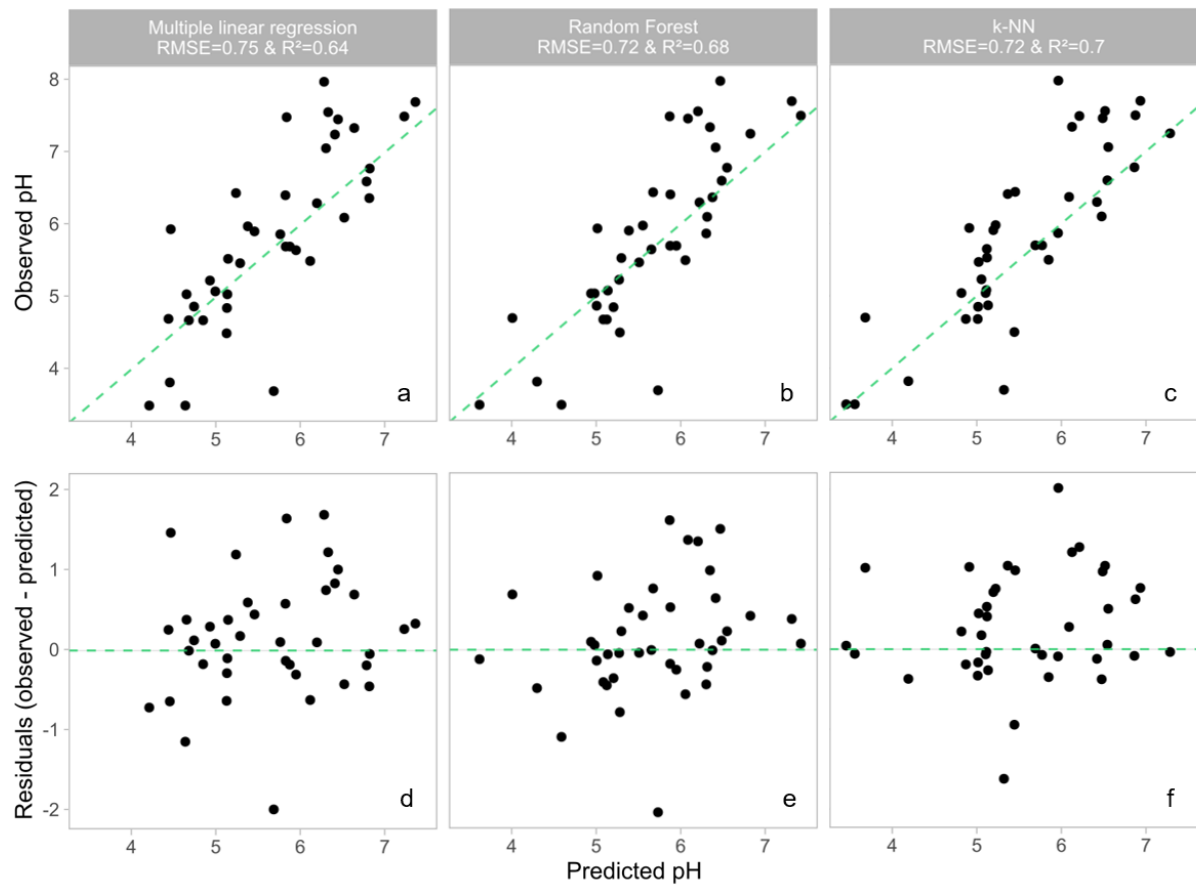


Figure 8. Results of the three different models tested to reconstruct the pH from 3-OH FA distribution: observed pH vs predicted pH for (a) the multiple linear regression model, (b) the random forest model, (c) the k-NN method. pH residuals plotted against the predicted pH for (d) the multiple linear regression model, (e) the random forest model and (f) the k-NN method.

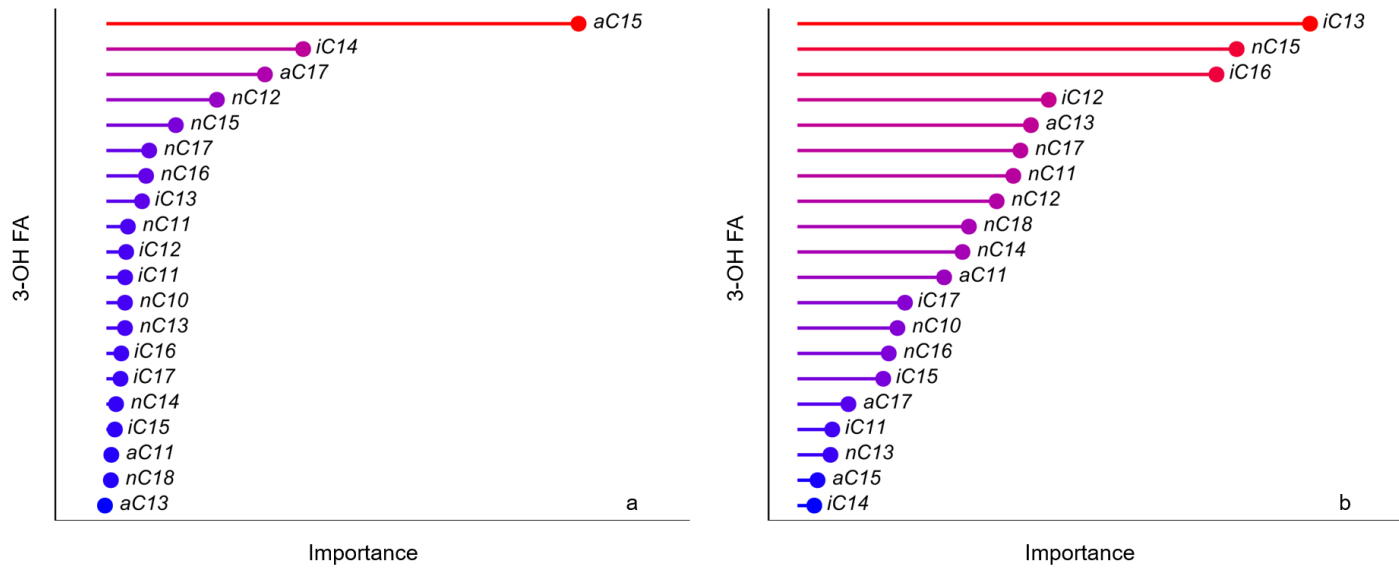


Figure 9. Importance (arbitrary unit) of the 3-OH FAs used to estimate (a) MAAT and (b) pH in the random forest models proposed in this study according to the permutation importance method (Breiman, 2001).

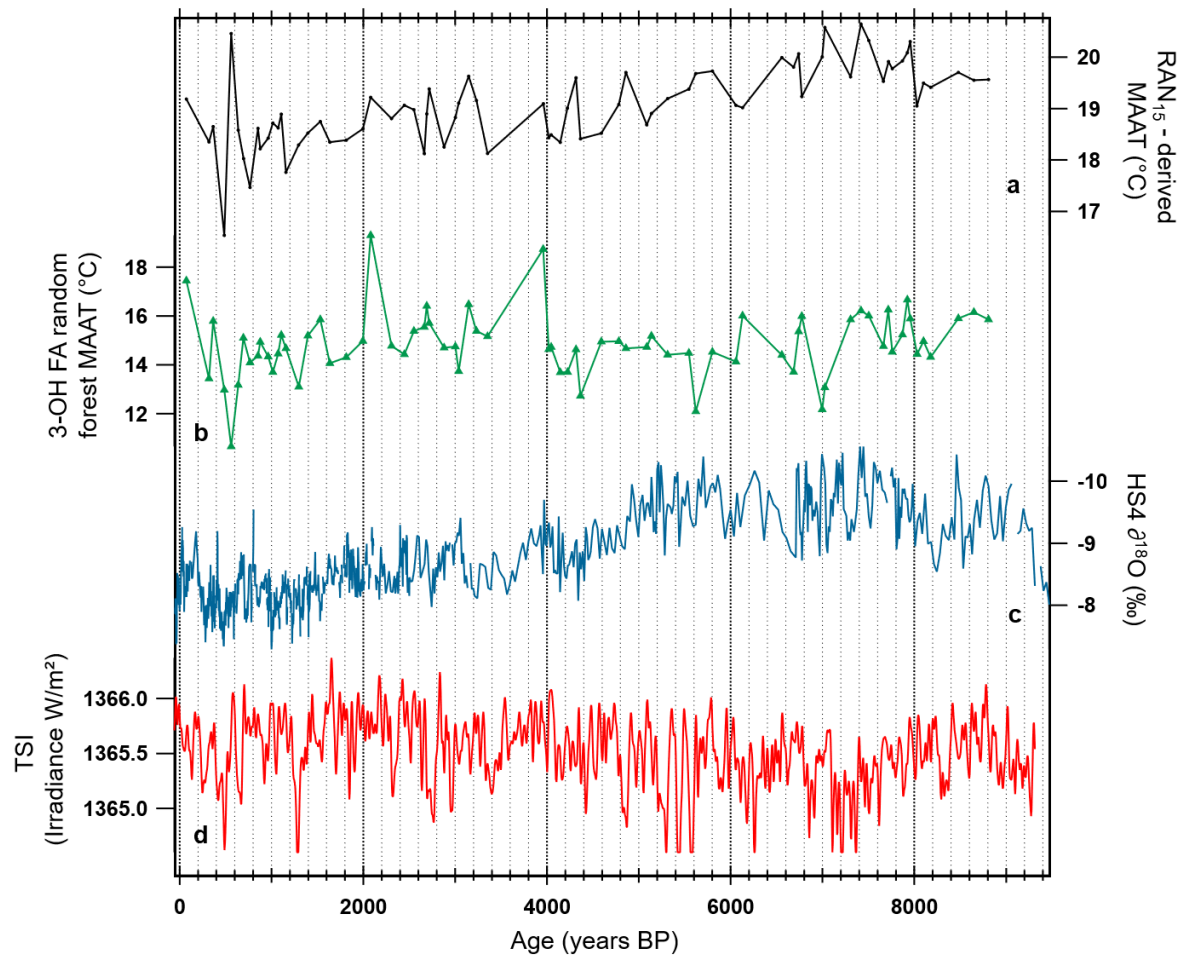


Figure 10. Comparison of the 3-OH FA model-MAAT record with other time-series and proxy records for the HS4 speleothem (Wang et al., 2018). (a) RAN₁₅-MAAT record reconstructed using a local Chinese calibration (Wang et al., 2016; Wang et al., 2018). (b) 3-OH FA random forest model-MAAT. (c) The CaCO₃ oxygen isotope record (Hu et al., 2008b). (d) Total solar irradiance (TSI; W/m²) during the Holocene (past 9300 years) based on a composite described in Steinhilber et al. (2009).

ID	Location	Altitude (m)	MAAT (°C)	pH	RAN ₁₅	RAN ₁₇	RIAN	MBT' _{5Me}	CBT'
1	Peruvian Andes	194	26.4	3.7	2.45	0.96	0.47	0.96	-1.09
2	Peruvian Andes	210	26.4	4	2.56	0.61	0.60	0.97	-1.92
3	Peruvian Andes	1063	20.7	4.7	3.46	0.70	0.54	0.98	-1.76
4	Peruvian Andes	1500	17.4	3.5	4.15	0.93	0.51	0.91	-1.55
5	Peruvian Andes	1750	15.8	3.6	5.30	1.32	0.51	0.92	-1.62
6	Peruvian Andes	1850	16	3.5	6.81	1.23	0.54	0.96	-1.76
7	Peruvian Andes	2020	14.9	3.4	7.00	1.19	0.54	0.95	-1.68
8	Peruvian Andes	2520	12.1	3.7	8.40	1.59	0.53	0.74	-1.42
9	Peruvian Andes	2720	11.1	3.6	8.42	1.73	0.48	0.83	-1.45
10	Peruvian Andes	3020	9.5	3.4	13.78	2.21	0.44	0.83	-1.21
11	Peruvian Andes	3200	8.9	3.5	6.91	2.35	0.37	0.71	-1.48
12	Peruvian Andes	3025	11.1	3.5	8.86	1.74	0.52	0.82	-1.66
13	Peruvian Andes	3400	7.7	3.4	9.10	2.39	0.40	0.71	-1.39
14	Peruvian Andes	3644	6.5	3.4	8.93	2.03	0.67	0.58	-1.21
15	Mt. Shegyla, Tibet	3106	8.9	5.53	6.22	2.02	0.51	0.59	-0.83
16	Mt. Shegyla, Tibet	3117	8.9	6.43	4.47	1.86	0.36	0.57	-0.35
17	Mt. Shegyla, Tibet	3132	8.8	6.01	4.07	1.72	0.43	0.61	-0.47
18	Mt. Shegyla, Tibet	3344	7.6	6.03	5.40	2.80	0.34	0.51	-0.67
19	Mt. Shegyla, Tibet	3355	7.5	5.87	4.09	2.71	0.23	0.44	-0.39
20	Mt. Shegyla, Tibet	3356	7.5	5.52	3.87	2.14	0.25	0.42	-0.70
21	Mt. Shegyla, Tibet	4030	3.7	5.21	8.21	3.64	0.43	0.49	-1.10
22	Mt. Shegyla, Tibet	4046	3.6	4.68	8.37	3.00	0.49	0.52	-1.17
23	Mt. Shegyla, Tibet	4050	3.6	4.61	8.94	2.47	0.50	0.44	-1.33
24	Mt. Shegyla, Tibet	3912	4.3	5.04	9.74	2.30	0.48	0.40	-2.39
25	Mt. Shegyla, Tibet	3918	4.3	4.68	8.67	1.80	0.56	0.45	-2.23
26	Mt. Shegyla, Tibet	4298	2.1	5.04	10.00	2.78	0.50	0.45	-2.04
27	Mt. Shegyla, Tibet	4295	2.2	4.87	12.17	3.90	0.50	0.42	-1.07
28	Mt. Shegyla, Tibet	4304	2.1	5.26	10.10	3.20	0.46	0.46	-1.14
29	Mt. Shegyla, Tibet	4479	1.1	5.26	10.11	3.42	0.52	0.35	-1.27
30	Mt. Shegyla, Tibet	4479	1.1	5.07	5.71	3.00	0.50	0.35	-0.84
31	Mt. Shegyla, Tibet	4474	1.1	5.24	7.88	3.65	0.42	0.32	-1.15
32	Mt. Pollino, Italy	0	18	6.78	2.71	1.19	0.15	0.50	0.31
33	Mt. Pollino, Italy	200	17	6.19	2.41	1.28	0.30	0.63	0.34
34	Mt. Pollino, Italy	400	16	6.13	4.26	2.29	0.22	0.58	0.35
35	Mt. Pollino, Italy	600	15	6.14	4.15	2.36	0.22	0.55	0.43
36	Mt. Pollino, Italy	800	14	4.53	3.34	2.77	0.34	0.51	-0.24
37	Mt. Pollino, Italy	1000	13	5.41	3.06	1.83	0.28	0.48	0.10
38	Mt. Pollino, Italy	1200	12	6.37	4.21	1.91	0.24	0.55	0.43
39	Mt. Pollino, Italy	1400	11	5.62	5.77	4.16	0.18	0.52	0.40
40	Mt. Pollino, Italy	1600	10	4.93	7.64	4.54	0.27	0.44	-0.13
41	Mt. Pollino, Italy	1800	9	4.91	3.45	3.17	0.25	0.45	-0.07
42	Mt. Pollino, Italy	2000	8	5.52	6.35	4.52	0.19	0.56	0.40
43	Mt. Pollino, Italy	2100	7.5	5.91	10.26	3.62	0.19	0.42	0.38
44	Mt. Pollino, Italy	2200	7	5.85	6.21	2.82	0.31	0.47	0.34
45	Chilean Andes	690	9.2	5.38	5.01	3.51	0.42	0.41	-0.80
46	Chilean Andes	870	8.9	5.62	5.21	2.43	0.39	0.49	-0.52
47	Chilean Andes	891	7.9	4.94	5.18	2.69	0.53	0.44	-0.94
48	Chilean Andes	915	NA	6.75	4.67	4.25	0.21	NA	NA
49	Chilean Andes	980	8.5	5.63	3.87	3.83	0.28	0.46	-0.66
50	Chilean Andes	985	5.8	4.67	6.41	3.12	0.48	0.41	-1.83
51	Chilean Andes	1125	6.0	5.00	3.83	4.18	0.46	0.42	-1.02
52	Chilean Andes	1151	6.0	5.89	4.74	2.89	0.33	0.43	-0.32
53	Chilean Andes	1196	7.1	5.79	5.70	4.07	0.34	0.43	-0.40
54	Chilean Andes	1385	NA	4.43	4.85	1.91	0.39	0.41	-2.28

Table 1. List of the soil samples collected along Mts. Shegyla, Pollino, Peruvian Andes and Chilean Andes, with corresponding altitude (m), MAAT (°C), pH and 3-OH FA/brGDGT-derived indices.

	Model	n (training)	n (test)	R ²	RMSE	Variance in residuals	Mean absolute error	Lower estimation limit	Upper estimation limit
MAAT (°C)	RAN ₁₅	-	168	0.37	5.5	29.8	4.0	-3.1	17.2
	RAN ₁₇	-	168	0.41	5.3	27.9	3.9	-4.3	17.0
	k-NN	128	40	0.77	3.1	9.4	2.3	0.5	25.0
	Multiple linear regression	128	40	0.79	3.0	9.2	2.3	-1.2	25.8
	Random forest	128	40	0.83	2.8	8.0	2.2	0.8	24.9
pH	RIAN	-	168	0.34	1.0	1.0	0.8	4.1	7.9
	k-NN	128	40	0.70	0.7	0.5	0.5	3.4	8.7
	Multiple linear regression	128	40	0.64	0.8	0.6	0.6	4.0	8.3
	Random forest	128	40	0.68	0.7	0.5	0.5	3.5	7.8

Table 2. Characteristics of the different models proposed in this study to estimate MAAT and pH: R², RMSE, variance of the residuals, mean absolute error (MAE) and the upper and lower limits of estimation. The "training" samples were used to develop the different machine learning models, which were then tested on a "test" sample set.